Real-time estimation and prediction of tire forces using digital map for driving risk assessment

Kun Jiang, Diange Yang, Shichao Xie, Zhongyang Xiao, Alessandro Corrêa Victorino, Ali Charara

Version of Record: https://www.sciencedirect.com/science/article/pii/S0968090X19311672
Manuscript_56676b57cb32983bd1468ab2ea16ae2e

Real-time Estimation and Prediction of Tire Forces Using Digital Map for Driving Risk Assessment

Kun Jiang [1,2], Diange Yang [1] , Shichao Xie [1] , Zhongyang Xiao [1] , Alessandro Corrêa Victorino [2], Ali Charara [2]

1 State Key Laboratory of Automotive Safety and Energy, Department of Automotive Engineering, Collaborative Innovation Center of Intelligent New Energy Vehicle, School of Vehicle and Mobility, Tsinghua University, Beijing, 100084.
jiangkun@tsinghua.edu.cn; ydg@tsinghua.edu.cn
2 Laboratoire Heudiasyc, CNRS UMR 7253, Sorbonne universités, Université de Technologie de Compiègne, France. acharara@hds.utc.fr

Abstract

This work aims to develop a driving risk warning system to enhance the road safety. Different from the existing lane departure warning system, speed limit warning system or collision warning system, the warning system proposed in this work focuses on the safety regarding vehicle's dynamics states. Many road accidents are caused by losing control of vehicle dynamics, such as the rollover, car drift and brake failure. First of all, the importance of monitoring vehicle dynamics states, especially the tire forces, is explained. Then the driving risk assessment criteria based on tire forces are developed in this work. The main contribution of this paper is the development of vehicle dynamics models and observers to estimate and predict individual tire forces using only low-cost sensors and ADAS (Advanced Driver Assistance Systems) map. The major new techniques developed in this study can be summarized in three aspects: 1) development of new vehicle dynamics models to estimate vertical, longitudinal, and lateral tire forces, 2) development of new nonlinear observers to minimize the estimation errors caused by sensor noises and model uncertainty, and 3) development of the tire forces prediction algorithm by taking advantage of digital map. The proposed warning system is validated by real vehicle experiments.

Keywords: vehicle dynamics; nonlinear observer; tire forces estimation and prediction; driving risk assessment; ADAS map.

1 Introduction

The potential ability to eliminate all road accidents is the most attractive point of developing intelligent connected vehicles. The large-scale use of fully autonomous driving vehicles in a smart city is a beautiful and exciting target proposed by many automotive companies and research institutes. The achievement of this target still needs lots of efforts in the next decades. However, improving the road safety is quite a critical and urgent task that should be accomplished as soon as possible. Many ADAS (Advanced Driver Assistance Systems) have already been introduced to the market and are saving people's lives. According to the report of the US Department of Transportation (NHTSA, 2013), of the vehicles equipped with both ABS(antilock brake system) and ESC(Electronic Stability Controller), 7.5% ran off the road, while of those equipped with neither ABS nor ESC, 14.6% ran off the road. ACC (adaptive cruise control) and AEB (autonomous emergency brake) are also proved to be effective in improving road safety, and mandatory installation of such ADAS systems is expected be legislated in many countries.

The role of ADAS is to help drivers avoid road accidents. One of the key difficulties in developing ADAS is the diagnosis of possible road accidents in the current instant, or even in the future instant. The earlier the ADAS could detect the possible accidents, the more time the driver could have to prepare and take reactions. The comparison of different ADAS is illustrated in Figure 1. In order to diagnose the possible accidents while it has not happened, the ADAS system needs to fulfill three tasks: 1, defining driving risk assessment criteria; 2, monitoring the current values of the parameters needed by the assessment; 3, predicting the future values of the parameters needed by the assessment. Furthermore, to cover the requirement of automated and connected vehicles, the range of vehicle dynamic state estimation need to extend (Guo et al. 2018).

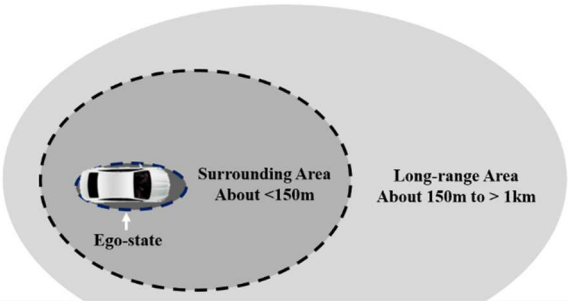

Typical ADAS System	Perception area	Reaction time before accident	Driving risk Assessment
ABS, ESP	Ego-state	<1s	Sideslip angle, slip ratio
AEB, ACC	Surrounding Area	<5s	Time to collision, distance to obstacle
ADAS navigation	Long-range Area	>5s	Speed limit sign, Sharp turning sign

Figure 1. Comparison of different ADAS regarding its perception area, reaction time and function mechanism

For the driving risk assessment, various methods are developed from different view points. In this paper, the evaluation of driving risk mainly refers to the assessment of rollover safety, longitudinal safety and lateral safety. In the literature (Bouton et al., 2007), the vehicle rollover phenomenon of light all-terrain vehicles is predicted with a rollover indicator. Rollover prediction method for heavy vehicles can be found in the literature (Imine et al., 2007). Different assessment methods of vehicle's longitudinal and lateral safety can be found in the literature (Rajamani, 2012; Reza, 2007; Pacejka, 2006). In the ABS system, the longitudinal safety is evaluated by the tire slip ratio. In the ESP system, the lateral safety is usually evaluated by the sideslip angle. They are designed to handle the situation that a dangerous tire slip has already happened, but not able to predict the potential dangers in a future instant. In some particular situation, such as high speed driving, even the ABS or ESP is not able to control the vehicle back to safe state, as it is too late to correct the driver's errors when the safety system is triggered. In the ACC and AEB system, the longitudinal safety is modeled with the position, speed and acceleration of the front vehicles or obstacles. Generally, it is reasonable to use the distance to obstacle to assess driving risk. Nevertheless, it is very difficult to define a threshold value that could ensure vehicle's safety in different situation. In fact, the safety distance varies with the driving situation. For example, the safety distance between vehicles is much larger for a heavy truck in a rainy day, compared with a small car in a sunny day. In order to provide a better assessment of vehicle safety, the relationships between vehicle dynamics states and vehicle safety have been discusses analyzed in (Ouahi et al., 2013; Dahmani et al, 2013; Wang et al., 2013, Kissai et al. 2018).

A remarkable point of this paper is that we propose to use tire forces to evaluate vehicle's safety. The motion of a car is usually considered by default to be controlled by steering wheel, brake, pedal or engine. Unfortunately, in some situation, for example on a slippery road, the steering wheel cannot effectively change the direction of vehicle and this usually leads to accidents. In addition, when the vehicle is driven on the inclined road, the vehicle dynamics is easier to enter the dangerous region leading to the instability of vehicle. Taking a further analysis of these cases, we can find that the vehicle motion is actually controlled by the tire-road contact forces. In Section 2, we will discuss how to use tire-road contact forces to evaluate vehicle's safety, including vertical safety, longitudinal safety and lateral safety.

After the definition of driving risk assessment criteria, the monitoring of tire forces is the next critical task that should be solved in this work. In order to assess vertical , longitudinal and lateral safety, the tire-road force in three directions of each wheel are required. Currently in the passenger cars, there is no available system for the monitoring of individual tire forces in three directions. However, lots of related research works can be found in the literature. We would like to conclude the current tire force monitoring methods as four types: direct measurement (Wang et al., 2013), estimation based on kinematics model (Ryu et al., 2004), estimation based on dynamics model (Milliken et al., 2003) and estimation based on state observers (Dahmani, 2013). In this work, we developed non-linear state observers to provide real-time estimation of tire forces with

higher accuracy and efficiency. The details about the real-time estimation will be presented in Section 3.

In order to gain more time for the driver to take reactions to avoid accidents or reduce damages, it is necessary to assess the driving risk in both the current road and the upcoming road. In the literature (Ghandour et al., 2011; Wang et al., 2013), the authors proposed to use the infrastructure on the road to communicate the environment information to the vehicle. Then the communication data is utilized to decide whether the current speed is safe to pass through the upcoming corner. The infrastructure-based method relies on the quality of V2I communication system and is expensive to cover a large area. It is not employed in this work. In this paper, we propose to retrieve road information from a digital map. The digital map has the advantage of being cost effective and being able to describe the static environment with high precision. It could provide a variety of useful information for the vehicle to make correct decisions to prevent accidents. The using of digital map to enable the prediction of tire forces can be divided into four steps: definition of ADAS map data structure, vehicle localization, map matching and map reading, which will be explained in Section 4.

Experimental tests have been implemented to validate our tire forces monitoring system. The driving risk assessment system is also tested to detect possible dangerous situation. The experimental results are presented in Section 5. Then conclusion and perspectives are given in Section 6.

2 Driving Risk Assessment

2.1 Tire fundamentals

Tires are the only vehicle components generating external forces that can be effectively manipulated to control vehicle motions. This important role of tires makes tire force modeling a crucial topic for vehicle control. In order to guarantee the optimal driving maneuvers in different road condition including slippery roads, it is important to be aware of the actual tire forces and the maximum attainable tire forces. In this way, we can decide whether the tire is at the imminence of losing control and whether the protection process should be activated. The tire-road contact can generate longitudinal force, lateral force and vertical force (F_x, F_y, F_z), and moments along three direction (M_x, M_y, M_z) allowing the car to accelerate/brake and to turn, as illustrated in the Figure 2.

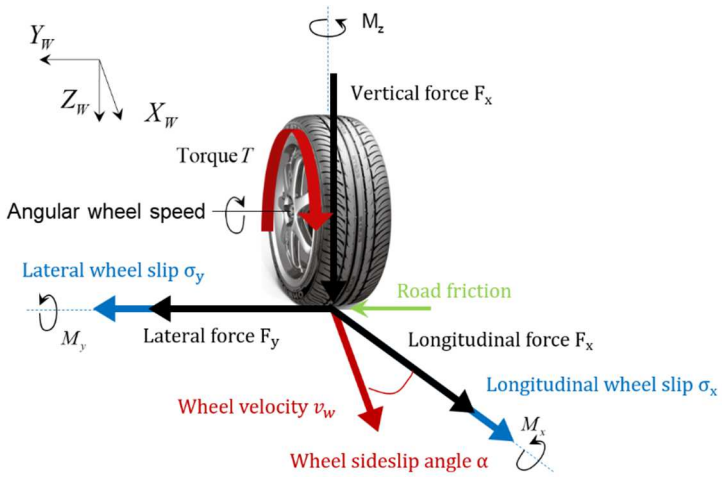

Figure 2. Illustration of terminology in tire models

The importance of tire to vehicle's safety is clearly recognized by the automotive industry. The lateral tire slip will result in car drift. The longitudinal tire slip will result in brake failure. The ABS and ESP systems are developed to detect and handle these dangerous situations. According to the mechanism of ABS and ESP introduced in (Rajamani, 2012; Reza, 2007; Pacejka, 2006), the tire state in these systems is assessed by the tire slip ratio and sideslip angle. The advantage of this assessment method is that it can detect the car drift and brake failure quickly and efficiently. However, its limitation is also obvious, it is designed for detect a dangerous situation that has already happened, which means the sideslip angle and tire slip ratio become significant. It is because the value of sideslip angle and slip ratio is very small and very hard to detect during normal driving situation.

Compared with tire slip ratio and tire sideslip angle, the tire forces can reflect the tire state more directly. Investigation has shown the influence of lateral tire force on vehicle lateral reliability and ride comfort (Li and He, 2016). Furthermore, by using tire forces, it is easier to detect potential tire slip. Nevertheless, there is no available sensors in ordinary passenger cars to directly measure tire forces for technical and economical reasons. The solution to this problem will be addressed in section 3. Assuming that the tire forces are available, the next subsection will introduce how to assess vehicle safety by using tire forces.

2.2 Risk assessment using tire forces

In order to evaluate vehicle's safety, we employ three risk assessment indexes: load transfer ratio (LTR), lateral skid ratio (LSR) and the brake failure ratio (BFR) (Imine et al., 2007). These risk assessments are based on the awareness of tire forces. The lateral load transfer ratio LTR is defined by using four wheel vertical forces as in Equation (1).

$$LTR = \frac{F_{z11} - F_{z12} + F_{z21} - F_{z22}}{F_{z11} + F_{z12} + F_{z21} + F_{z22}} \qquad (1)$$

The lateral skid ratio LSR represents the loss of adhesion resulting in the lateral drift. The lateral skid ratio is defined by road friction coefficient and tire forces, as in Equation (2).

$$LSR_{ij} = 1 - \left|\frac{\mu_{max} - \mu_{ij,lat}}{\mu_{max}}\right| \qquad \mu_{ij,lat} = \left|\frac{F_{yij}}{F_{zij}}\right| \tag{2}$$

where μ_{max} is the threshold of safe friction, $\mu_{ij,lat}$ is the equivalent lateral friction coefficient.

The brake failure ratio BFR represents the loss of adhesion resulting in the longitudinal tire slip. The brake failure ratio is defined by road friction coefficient and tire longitudinal forces, as follow:

$$BFR_{ij} = 1 - \left|\frac{\mu_{max} - \mu_{ij,lon}}{\mu_{max}}\right| \qquad \mu_{ij,lon} = \left|\frac{F_{xij}}{F_{zij}}\right| \tag{3}$$

3 Real-time Estimation of Tire Forces

3.1 Related works in estimation of tire forces

The related tire force monitoring methods in the literature can be concluded as four types: direct measurement, estimation based on kinematics model, estimation based on dynamics model and estimation based on state observers.

1) Direct measurement

In (Nam et al, 2013), the author employed four force sensors to measure only the lateral forces. However, it is not realistic to use this method to measure all three directional components of each tire. In (Dherbomez et al., 2013), the author installed four expensive wheel transducers, each of which could measure the six components (three forces and three torques in the longitudinal, lateral, and vertical directions) of the road–tire contact force system. However, the price and complexity of this system make it hardly acceptable for automotive manufacturers. Furthermore, limited by the sensor's physical mechanism, the direct measurements are sensitive to the influence of the environment and can only work under particular conditions.

2) Vehicle kinematics model

According to the kinematic motion of a vehicle, the tire slip state can be expressed using Figure 3 and Equation (4). Then, the sideslip angle can be obtained by numerical integration of inertial sensors (Reza, 2007). The advantage of the kinematics model-based method is that it is independent of the tire properties, road friction, and other vehicle parameters. Thus, it can achieve good robustness against the vehicle's unmodeled dynamics and parameters as well as variations under tire-road conditions. Nevertheless, the integration process accumulates the sensor errors, especially for the lateral acceleration signal, which results in a huge bias in the final estimation result.

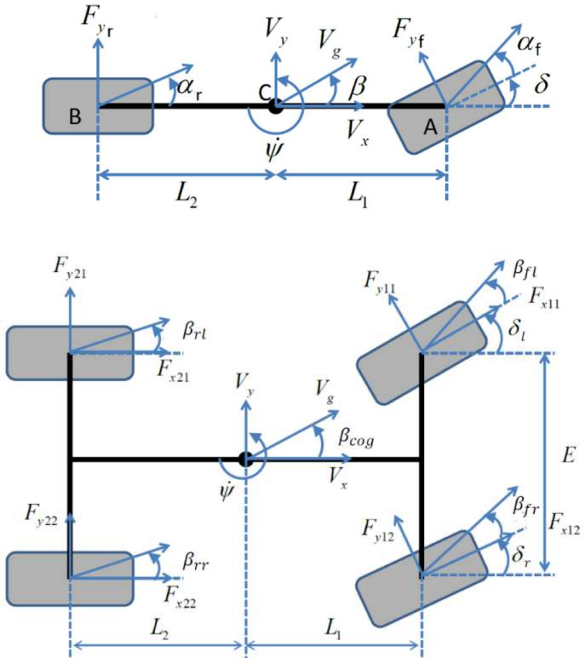

Figure 3. Bicycle model and four-wheel model for describing vehicle dynamics

$$\beta_{cdg} = \frac{a_y}{v_x} - \dot{\psi} \qquad (4)$$

where a_y is the lateral acceleration, v_x is the longitudinal velocity, $\dot{\varphi}$ is the yaw rate and β_{cog} is the sideslip angle of vehicle at center of gravity (COG).

3) Vehicle dynamics model

In this method, the relations among the sideslip angle, tire forces, and vehicle motion are described by the vehicle dynamics models and tire models (Rajamani, 2012; Reza, 2007; Pacejka, 2006). To achieve real-time practical applications, this method usually adopts a simplified but effective model, for example, the bicycle model. However, the simplified model error is significant, especially during extreme driving maneuvers. The main advantage of this method is that it does not accumulate sensor bias and can achieve accurate estimation in normal driving maneuvers.

4) State observer

To overcome the shortcomings of the kinematics model and the dynamics model method, several studies have been proposed to construct a state observer, also called a virtual sensor, to provide the best estimation. The linear observer deals with a linear model, such as the Luenberger observers, recursive least squares algorithms, and Kalman filters (KFs) (Li et al., 2014; Klomp et al., 2014; Li et al., 2014; Gadola et al., 2014). The nonlinear observer is developed to deal with nonlinear vehicle dynamics models. A fuzzy observer that utilizes the fuzzy model with T–S fuzzy rules to represent the nonlinear vehicle model was proposed to estimate the vehicle slip angle (Ouahi et al., 2013). The extended Kalman filter is an effective method to deal with nonlinear models, as it provides a linear approximation of such models (Wang et al., 2013, Reina et al. 2017, Lee et al. 2018). Besides, the EKF has been proved able to cover the time-variant vehicle parameters (Reina and Messina, 2018).

In this study, the estimation of tire forces is based on the state observer method and the observer is developed according to the KF algorithm (including linear KF, extended KF, and unscented KF) and particle filter algorithm. Although many KF-based observers have been proposed in the literature, estimation of the lateral dynamics in an accurate and robust way is still challenging. Generally, the existent KF observers can be improved in two aspects:

• further development of vehicle models that can accurately describe all dynamics of interest while being as simple as possible.

• creative construction of observers that can compensate for the model and sensor errors to the maximum possible extent.

This section proposes modifications in both these aspects.

3.2 Further development of vehicle dynamics models

Vehicle dynamics has been an intense research subject for more than a hundred years. Developing vehicle models that accurately describe all dynamics of interest while being as simple as possible is the main challenge in the so-far developed vehicle state observers. Consider a four-wheel vehicle model, as illustrated in the Figure 3. The longitudinal, lateral and vertical force of a tire are noted as F_{xij}, F_{yij}, F_{zij} respectively. The index ij represents the identity of the corresponding tire. In the literature, a vehicle's planar dynamics are expressed by

$$\begin{bmatrix} m\left(\dot{v}_x - \dot{\psi} v_y\right) \\ m\left(\dot{v}_y + \dot{\psi} v_x\right) \\ m\dot{v}_z \end{bmatrix} = \begin{bmatrix} 0 \\ 0 \\ mg \end{bmatrix} + \sum \begin{bmatrix} F_{xij}\cos\delta_{ij} - F_{yij}\sin\delta_{ij} \\ F_{xij}\sin\delta_{ij} + F_{yij}\cos\delta_{ij} \\ F_{zij} \end{bmatrix}$$

$$\begin{bmatrix} 0 \\ 0 \\ I_z\ddot{\psi} \end{bmatrix} = \begin{bmatrix} y_{ij}F_{zij} - z_{ij}\left(F_{xij}\sin\delta_{ij} + F_{yij}\cos\delta_{ij}\right) \\ -x_{ij}F_{zij} + z_{ij}\left(F_{xij}\cos\delta_{ij} - F_{yij}\sin\delta_{ij}\right) \\ x_{ij}\left(F_{xij}\sin\delta_{ij} + F_{yij}\cos\delta_{ij}\right) \\ -y_{ij}\left(F_{xij}\cos\delta_{ij} - F_{yij}\sin\delta_{ij}\right) \end{bmatrix} \quad (5)$$

where v_x, v_y, $\dot{\varphi}$, δ indicate the measured longitudinal speed, lateral speed, yaw velocity and steering angle, respectively. I_z is the vehicle's moment of inertia around z-axis. g is the standard gravity on earth.

However, Equation (5) is inadequate for obtaining individual tire forces in three directions (F_{xij}, F_{yij}, F_{zij}). Therefore, we propose additional models about vertical, longitudinal and lateral vehicle dynamics as follow.

3.2.1 Consideration of suspension's roll and pitch movements

Both the pitch and roll motion of suspension are taken into account to model the vertical vehicle dynamics. The rotation of the vehicle body with respect to vehicle-

frame-fixed axes is given by the Euler angles (ψ_v, θ_v, φ_v), where ψ_v is rotation angle about the z -axis, θ_v is rotation about the y-axis (pitch angle) and φ_v is rotation about the x-axis (roll angle).

The suspension can be regarded as a damping system. For the pitch motion, the suspension is characterized by a pitch stiffness K_θ and pitch damping coefficient C_θ. Similarly, for the roll motion, the suspension can be represented by a roll stiffness K_φ and roll damping coefficient C_φ. The torques generated by the vehicle suspension could be calculated as

$$\begin{aligned} M_{x,sus} &= C_\varphi \dot{\varphi}_v + K_\varphi \varphi_v \\ M_{y,sus} &= C_\theta \dot{\theta}_v + K_\theta \theta_v \end{aligned} \tag{6}$$

where $M_{x,sus}$, $M_{y,sus}$ are the torque about x-axis and y-axis respectively.

Then, the variation in tire vertical force during the motion can be explained by the torque of suspension, as follows:

$$\begin{aligned} F_{z11,s} &= \frac{1}{2} m a_z \frac{L_2}{L} - \frac{1}{2L} M_{y,sus} - \frac{L_2}{e_1 L} M_{x,sus} \\ &\quad + \frac{L_2}{e_1 L^2 mg} M_{x,sus} M_{y,sus} \\ F_{z12,s} &= \frac{1}{2} m a_z \frac{L_2}{L} - \frac{1}{2L} M_{y,sus} + \frac{L_2}{e_1 L} M_{x,sus} \\ &\quad - \frac{L_2}{e_1 L^2 mg} M_{x,sus} M_{y,sus} \\ F_{z21,s} &= \frac{1}{2} m a_z \frac{L_1}{L} + \frac{1}{2L} M_{y,sus} - \frac{L_1}{e_2 L} M_{x,sus} \\ &\quad - \frac{L_1}{e_2 L^2 mg} M_{x,sus} M_{y,sus} \\ F_{z22,s} &= \frac{1}{2} m a_z \frac{L_1}{L} + \frac{1}{2L} M_{y,sus} + \frac{L_1}{e_2 L} M_{x,sus} \\ &\quad + \frac{L_1}{e_2 L^2 mg} M_{x,sus} M_{y,sus} \end{aligned} \tag{7}$$

where e_1 and e_2 are the width of the front axle and rear axle respectively.

The advantage of this model is that it is sensitive to suspension motion and is independent of the inertial sensors.

3.2.2 New models for lateral and longitudinal tire forces

While some model-less estimators were applied to improve the robustness (Rezaeian et al. 2015), the common method to obtain lateral and longitudinal tire forces in literature is to employ tire slip based tire models, such as the linear tire model, Brush tire model, LuGre model (Ehsan et al. 2017), Dugoff's tire model, and Pacejka's magic tire model (Rajamani, 2012; Reza, 2007; Pacejka, 2006). The linear tire model is

accused of being over simplified. On the contrary, Dugoff's and Pacejka's tire models are very complex and have many parameters to be configured before application. In addition, the accuracy of these models is highly dependent on the effect of the tire slip measurement. However, the tire slip is such a small quantity that its measurement can be easily disturbed by sensor errors. Therefore, we propose novel models to calculate tire forces without tire slip.

In this study, we find that forces at the left and right tires are related, and we try to model this relation. We use the following notations: the transfer of lateral force at front axle is indicated by $T_{Fy,f}$ and that at rear axle is indicated by $T_{Fy,r}$; the transfer of longitudinal force at front axle is indicated by $T_{Fx,f}$ and that at the rear axle is indicated by $T_{Fx,r}$. They are defined as follows:

$$\begin{bmatrix} T_{Fy,f} \\ T_{Fy,r} \\ T_{Fx,f} \\ T_{Fx,r} \end{bmatrix} = \begin{bmatrix} F_{y11} - F_{y12} \\ F_{y21} - F_{y22} \\ F_{x11} - F_{x12} \\ F_{x21} - F_{x22} \end{bmatrix} \tag{8}$$

The value of $T_{Fy,f}$, $T_{Fy,r}$, $T_{Fx,f}$, $T_{Fx,r}$ can be obtained by employing the Brush model. The final calculation result is approximated by

$$\begin{bmatrix} T_{Fy,f} \\ T_{Fy,r} \\ T_{Fx,f} \\ T_{Fx,r} \end{bmatrix} = \begin{bmatrix} a_1(F_{z11} + F_{z12})\delta + a_2 \dfrac{F_{z11} - F_{z12}}{F_{z11} + F_{z12}} \left(F_{y11} + F_{y12}\right) \\ a_3 \dfrac{F_{z21} - F_{z22}}{F_{z21} + F_{z22}} \left(F_{y21} + F_{y22}\right) \\ a_4(F_{z11} + F_{z12})\delta + a_5 \dfrac{F_{z11} - F_{z12}}{F_{z11} + F_{z12}} (F_{x11} + F_{x12}) \\ a_6(F_{z21} - F_{z22}) \end{bmatrix} \tag{9}$$

where $a_1 F_{zf}\delta$ represents the force difference caused by the steering angle, $\frac{F_{z21}-F_{z22}}{F_{z21}+F_{z22}} F_{yf}$ represents the force difference caused by the load transfer.

With the proposed models in Equation (5) (7) (8) (9), the tire slip is no longer needed for computing the tire forces. Instead, the tire forces are computed with vertical load transfer, velocity, and yaw rate, which can be easily obtained using low-cost sensors.

3.3 Observer design

This subsection describes the observer devoted to tire forces (vertical, lateral, and longitudinal forces). The need of observers is motivated by the fact that the open-loop estimation is significantly influenced by the sensor noises and model errors. To minimize the inevitable errors and obtain the optimal estimation, observer techniques are employed. The observers we proposed are based on the Kalman Filter algorithm, including linear Kalman filter, extended Kalman filter (EKF) and unscented Kalman filter (UKF). The general KF algorithm is expressed by Equation (10).

$$
\begin{gathered}
Prediction with models: \\
\hat{X}_{k+1|k} = A\hat{X}_{k|k} + BU_{k+1} \\
P_{k+1|k} = AP_{k|k}A^T + Q_{k+1|k} \\
K_{k+1} = P_{k+1|k}H^T(HP_{k+1|k}H^T + R_{k+1|k})^{-1} \\
Update with measurements: \\
\hat{X}_{k+1|k+1} = \hat{X}_{k+1|k} + K_{k+1}(z_{k+1} - H\hat{X}_{k+1|k}) \\
P_{k+1|k+1} = (I - K_{k+1}H)P_{k+1|k}
\end{gathered} \tag{10}
$$

Where $\hat{X}_{k|k}$, $\hat{X}_{k+1|k}$ represents the state of system at time k and $k+1$ respectively. U represents the control vector. A, B represents the state transfer matrix and control matrix separately. P represents the covariance matrix between predicted and real values and Q represents the system noise covariance. K is Kalman gain matrix, H is observation transformation matrix and R is the observation noise covariance.

The entire tire force estimation process is divide the into four blocks, as shown in Figure 4. Each of the four observers will concentrate at one estimation target. The first observer is an Extended Kalman filter to estimate the vertical forces at each wheel. The estimation result of the first block will be regarded as a measurement in other blocks. The second observer is an Unscented Kalman filter to estimate the lateral forces. The unscented Kalman filter is employed to minimize the errors caused by the high non-linearity of tire's nature. The third observer is for the estimation of the longitudinal forces. The last observer is for the estimation of side slip angle. The strategy of using cascaded observers allows us to avoid the observability problems, furthermore it can enable the estimation process to be carried out in a simple and practical way. When all the states are observed in one observer, the covariance's value of each state is highly correlated to each other. It will be very hard to find which covariance value is not correct when the estimation is not good. With the cascaded observers, we can check the quality of vertical, longitudinal and lateral force estimation respectively. The observability of each observer is analysed by using equation (11):

$$
\begin{cases} observable & if\ \ rang(\{O\}) = m; \\ unobservable & if\ \ rang(\{O\}) < m; \end{cases} \quad with\ \{0\}
$$

$$
= \begin{pmatrix} C \\ CA \\ CA^2 \\ \vdots \\ CA^m \end{pmatrix} \tag{11}
$$

where A is the prediction matrix, C is the observation matrix, m is the dimension of the state vector, O is the observability matrix. The system is observable with the condition that the rank of above observability matrix is equal to the dimension of the state vector.

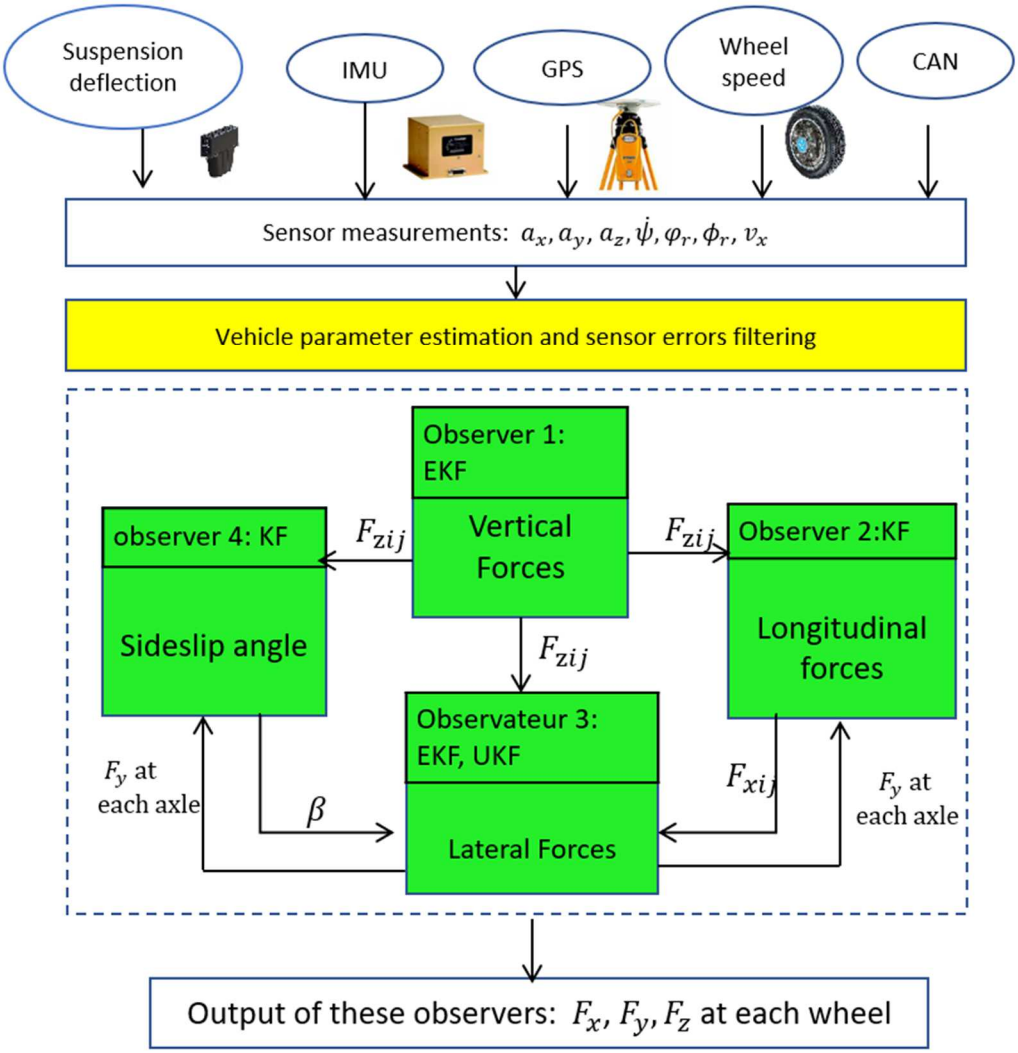

Figure 4. Overall algorithm of the tire force estimation process

Observer for tire's vertical force O_{Fz}

$$\begin{bmatrix} \dot{F}_{z11} \\ \dot{F}_{z12} \\ \dot{F}_{z21} \\ \dot{F}_{z22} \end{bmatrix} = 0^{4\times4} \begin{bmatrix} F_{z11} \\ F_{z12} \\ F_{z21} \\ F_{z22} \end{bmatrix} + Q_1(noise) \tag{12}$$

$$\begin{bmatrix} ma_z \\ F_{z11,k} \\ F_{z12,k} \\ F_{z21,k} \\ F_{z22,k} \end{bmatrix} = \begin{bmatrix} 1 & 1 & 1 & 1 \\ 1 & 0 & 0 & 0 \\ 0 & 1 & 0 & 0 \\ 0 & 0 & 1 & 0 \\ 0 & 0 & 0 & 1 \end{bmatrix} \begin{bmatrix} F_{z11} \\ F_{z12} \\ F_{z21} \\ F_{z22} \end{bmatrix} + R_1(noise)$$

where τ_1 is the time constant that the suspension need to develop the vertical force. $F_{zij,c}$ is obtained by Equation (7). The parameters of vehicle are supposed to be constants.

To implement the Kalman filter expressed in equation (10), the prediction matrix and the observation matrix are extracted.

$$\mathbf{A}_{Fz} = \begin{bmatrix} 1 & 0 & 0 & 0 \\ 0 & 1 & 0 & 0 \\ 0 & 0 & 1 & 0 \\ 0 & 0 & 0 & 1 \end{bmatrix}, \qquad \boldsymbol{C}_{Fz} = \begin{bmatrix} 1 & 1 & 1 & 1 \\ 1 & 0 & 0 & 0 \\ 0 & 1 & 0 & 0 \\ 0 & 0 & 1 & 0 \\ 0 & 0 & 0 & 1 \end{bmatrix} \tag{13}$$

For the observability, we can find that the observation matrix of vertical force in equation (13), $\boldsymbol{C}_{Fz}$, is already full rank. Then the observability evaluation matrix is sure to be full rank.

The observation models mainly come from equation (7), which enables us have direct estimation of vertical forces of four tires. In addition, we know that the total of four tire forces is directly related to the vehicle's mass and vertical acceleration. Then we can have 5 equations for the observation, as shown in equation (12).

Observer for tire's lateral force $\boldsymbol{O}_{\boldsymbol{Fy}}$

$$\begin{bmatrix} \dot{F}_{y11} \\ \dot{F}_{y12} \\ \dot{F}_{y21} \\ \dot{F}_{y22} \end{bmatrix} = \frac{1}{\tau}\left(\begin{bmatrix} f_{Tire,y}(\alpha_{11}, F_{z11}) \\ f_{Tire,y}(\alpha_{12}, F_{z12}) \\ f_{Tire,y}(\alpha_{21}, F_{z21}) \\ f_{Tire,y}(\alpha_{22}, F_{z22}) \end{bmatrix} - \begin{bmatrix} F_{y11} \\ F_{y12} \\ F_{y21} \\ F_{y22} \end{bmatrix} \right) + Q_2(noise)$$

$$\begin{bmatrix} ma_x - F_{xf}\cos\delta \\ ma_y - F_{xf}\sin\delta \\ I_z\ddot{\psi} - M_{Fx} - L_1\sin\delta F_{xf} \\ T_{Fy,f} \\ T_{Fy,r} \end{bmatrix} = \begin{bmatrix} -\sin\delta & -\sin\delta & 0 & 0 \\ \cos\delta & \cos\delta & 1 & 1 \\ L_1\cos\delta & L_1\cos\delta & -L_2 & -L_2 \\ 1 & -1 & 0 & 0 \\ 0 & 0 & 1 & -1 \end{bmatrix} \begin{bmatrix} F_{y11} \\ F_{y12} \\ F_{y21} \\ F_{y22} \end{bmatrix} + R_2(noise) \tag{14}$$

where $f_{Tire,y}(\alpha, F_{wz})$ is the static lateral tire forces calculated by Dugoff model. The detailed expression of Dugoff's model can be found in (Wang et al., 2013).

The prediction matrix and the observation matrix are extracted.

$$\mathbf{A}_{Fy} = \begin{bmatrix} 1-\frac{\Delta t}{\tau} & 0 & 0 & 0 \\ 0 & 1-\frac{\Delta t}{\tau} & 0 & 0 \\ 0 & 0 & 1-\frac{\Delta t}{\tau} & 0 \\ 0 & 0 & 0 & 1-\frac{\Delta t}{\tau} \end{bmatrix}$$

$$\boldsymbol{C}_{Fy} = \begin{bmatrix} -sin\delta & -sin\delta & 0 & 0 \\ cos\delta & cos\delta & 1 & 1 \\ L_1 cos\delta & L_1 cos\delta & -L_2 & -L_2 \\ 1 & -1 & 0 & 0 \\ 0 & 0 & 1 & -1 \end{bmatrix} \tag{15}$$

For the observability, we can find that the observation matrix of lateral force in equation (15), $\boldsymbol{C}_{Fy}$, is already full rank. Then the observability evaluation matrix is

sure to be full rank.

The first and second rows of $\boldsymbol{C}_{Fy}$ represent the total tire forces in the longitudinal and lateral directions, the third row of $\boldsymbol{C}_{Fy}$ represents the total moment generated by the lateral tire forces. They can be found in equation (5). The fourth and fifth rows of $\boldsymbol{C}_{Fy}$ are the difference of lateral forces between right and left wheels, which are modeled by equation (9).

Observer for tire's longitudinal force $\boldsymbol{O_{Fx}}$

$$\begin{bmatrix} \dot{F}_{xw11} \\ \dot{F}_{xw12} \\ \dot{F}_{xw21} \\ \dot{F}_{xw22} \\ \dot{M}_{Fx} \end{bmatrix} = 0^{5\times5} \begin{bmatrix} F_{x11} \\ F_{x12} \\ F_{x21} \\ F_{x22} \\ M_{Fx} \end{bmatrix} + Q_3(noise) \tag{16}$$

$$\begin{bmatrix} \dfrac{(ma_x + F_{yf}\sin\delta)}{\cos\delta} \\ F_{xr} \\ T_{Fx,f} \\ T_{Fx,r} \\ 0 \end{bmatrix} = \begin{bmatrix} 1 & 1 & 1 & 1 & 0 \\ 0 & 0 & 1 & 1 & 0 \\ 1 & -1 & 0 & 0 & 0 \\ 0 & 0 & 1 & -1 & 0 \\ \dfrac{E}{2} & -\dfrac{E}{2} & \dfrac{E}{2} & -\dfrac{E}{2} & 1 \end{bmatrix} \begin{bmatrix} F_{x11} \\ F_{x12} \\ F_{x21} \\ F_{x22} \\ M_{Fx} \end{bmatrix} + R_3(noise)$$

where F_{yf} is the resultant lateral force at front axle, it is obtained from the former observer. F_{xr} is the resultant longitudinal force in the rear axle, it is directly related to the brake pressure, normally, it is a constant value.

The prediction matrix and the observation matrix are extracted.

$$\mathbf{A}_{Fx} = \begin{bmatrix} 1 & 0 & 0 & 0 & 0 \\ 0 & 1 & 0 & 0 & 0 \\ 0 & 0 & 1 & 0 & 0 \\ 0 & 0 & 0 & 1 & 0 \\ 0 & 0 & 0 & 0 & 1 \end{bmatrix}$$

$$\boldsymbol{C}_{Fx} = \begin{bmatrix} 1 & 1 & 1 & 1 & 0 \\ 0 & 0 & 1 & 1 & 0 \\ 1 & -1 & 0 & 0 & 0 \\ 0 & 0 & 1 & -1 & 0 \\ e_1/2 & -e_1/2 & e_2/2 & -e_2/2 & 1 \end{bmatrix} \tag{17}$$

For the observability, we can find that the observation matrix of longitudinal force, $\boldsymbol{C}_{Fx}$, is already full rank. Then the observability evaluation matrix is sure to be full rank.

The first row of $\boldsymbol{C}_{Fx}$, is obtained by using equation (5). The second and the fifth rows of $\boldsymbol{C}_{Fx}$, are obtained through their physical definitions. The third and fourth row of $\boldsymbol{C}_{Fx}$, are the difference of lateral forces between right and left wheels, which are modeled by equation (9).

Observer for vehicle's sideslip angle O_β

$$\begin{bmatrix} \ddot{\beta}_{cog} \\ \dot{\beta}_{cog} \\ \dot{v}_y \end{bmatrix} = \begin{bmatrix} 0 & 0 & 0 \\ 0 & -\frac{C_f + C_r}{m_v v_x} & 0 \\ 0 & 0 & 0 \end{bmatrix} \begin{bmatrix} \dot{\beta}_{cog} \\ \beta_{cog} \\ v_y \end{bmatrix} + \begin{bmatrix} 0 \\ [-1 + \frac{L_2 C_r - L_1 C_f}{m_v v_x^2}]\dot{\psi} \\ 0 \end{bmatrix} + cov(noise) \tag{18}$$

$$\begin{bmatrix} \beta_{best} \\ \frac{a_y - g\sin\varphi_r}{v_x} - \dot{\psi} \\ 0 \end{bmatrix} = \begin{bmatrix} 0 & 1 & 0 \\ 1 & 0 & 0 \\ 0 & v_x & -1 \end{bmatrix} \begin{bmatrix} \dot{\beta}_{cog} \\ \beta_{cog} \\ v_y \end{bmatrix} + cov(noise)$$

The measurements we used in this block are the accelerations and suspension deflections. β_{best} is the sideslip angle obtained by analyzing the less-slip tire, the details have been introduced in (Jiang et al., 2016).

The prediction matrix and the observation matrix are extracted.

$$\mathbf{A}_\beta = \begin{bmatrix} 1 & 0 & 0 \\ 0 & 1 - \Delta t \frac{C_f + C_r}{m_v v_x} & 0 \\ 0 & 0 & 1 \end{bmatrix} \tag{19}$$

$$\boldsymbol{C}_\beta = \begin{bmatrix} 0 & 1 & 0 \\ 1 & 0 & 0 \\ 0 & v_x & -1 \end{bmatrix}$$

4 Prediction of tire forces using ADAS map

In order to make time for correcting driving behaviors, especially when driving at high speed, it seems very appealing for us to predict an impending dangerous event and react before the danger occurs. A digital map contains lots of useful information about the upcoming road for enhancement of road safety (Jiménez et al. 2009). A popular application of digital map is the in-vehicle navigation system, which could remind the drivers about the speed limits of the road. In the near future, the role of digital map would be much more important, if more information are stored in the map, such as the curvature and other geometry information of the road. In this case, the digital map is also called as ADAS map for its ability to assist drivers. Some example of applying the ADAS map can be found in (Durekovic et al., 2011). This section introduces a new safety system to predict the tire forces based on the use of ADAS maps.

4.1 ADAS map data structure

The road information that are useful for the prediction of tire forces are listed in Table 1. We only attribute these road information to the critical points (CPs) where the road condition changes a lot, such as roundabout, slippery region or traffic light stop. After the CPs are defined, the vehicle path could be represented by the CPs and the corridors between two CPs (Victorino et al, 2003), as illustrated in Table 2.

Table 1 Tags attributed to Critical Points

Longitude Position	Latitude Position	Altitude
x	y	h
Road Direction	Curvature	Vertical curvature
ψ_r	κ	ρ
Road Friction	Bank Angle	Slope Angle
μ	φ	θ
ID in map	Number of lanes	Number of roads
Id_{map}	N_{lane}	N_{road}

Table 2. Tags attributed to Corridors

Id of Beginning CP	Id of Ending CP	Length of Corridor
Id_0	Id_n	L_{corr}
Id of corridor	Curve or Line	Stop or Not
Id_{way}	R_{curve}={0,1}	R_{stop}={0,1}

The road information of a point in the map can be obtained by

$$Road_{Px} = \left(1 - \frac{L_x}{L_{road}}\right) Road_{CP0} + \frac{L_x}{L_{road}} Road_{CP1} \qquad (20)$$

where $Road_{CP0}$ and $Road_{CP1}$ indicates the road geometry information of start and end points of a corridor, respectively. L_x is the length between the current position and CP_0.

4.2 Map reading

To read required information from the map, the vehicle must be localized in the map. Map-matching process were developed using GPS data (Li et al. 2013, Quddus and Washington 2015). Lane-level localization can be achieved by incorporating road width information with GPS data (Sharath et al.2019). However, the GPS signal is not always available. The vehicle location is observed by the Extended Kalman filter algorithm to compensate the possible errors caused by signal lost, as shown in Equation (21).

Process model

$$\begin{bmatrix} \dot{X} \\ \dot{Y} \\ \dot{v}_x \\ \dot{\psi} \\ \ddot{\psi} \end{bmatrix} = \begin{bmatrix} \sin(\psi) \cdot v_x \\ \cos(\psi) \cdot v_x \\ a_x - \mathrm{g}\sin\theta \\ \dot{\psi} \\ 0 \end{bmatrix} + noise \tag{21}$$

Observation model:

$$\begin{bmatrix} X_{gps} \\ Y_{gps} \\ v_{gps} \\ \psi_{gps} \\ v_{wheel} \\ \dot{\psi}_{gyro} \end{bmatrix} = \begin{bmatrix} 1 & 0 & 0 & 0 & 0 \\ 0 & 1 & 0 & 0 & 0 \\ 0 & 0 & 1 & 0 & 0 \\ 0 & 0 & 0 & 1 & 0 \\ 0 & 0 & 1 & 0 & 0 \\ 0 & 0 & 0 & 0 & 1 \end{bmatrix} \begin{bmatrix} X \\ Y \\ v_x \\ \psi \\ \dot{\psi} \end{bmatrix} + noise$$

where X_{gps}, Y_{gps}, v_{gps}, v_{whell}, ψ_{gps}, $\dot{\psi}_{gyro}$ are the measurement of GPS receiver and inertial units, ψ is the clockwise angle between the north and the vehicle direction. After the localization, we can obtain the road information of the current position and the future position, by combining Equation (21) and the following equation:

$$L_x = f\left(X, Y, L_{pred}\right) \tag{22}$$

where X, Y are the current position, L_{pred} is the distance ahead of vehicle, the details about f are provided in (Jiang et al, 2016).

Then according to the road information from the ADAS map, the kinematic parameters of the vehicle can be predicted as

$$\begin{aligned} ax_{map} &= dv_x/dt + g\sin\theta_{map} \\ ay_{map} &= v_x^2\kappa_{osm} + g\sin\varphi_{map} \\ az_{map} &= v_x^2\rho_{map} + g\cos\theta_{map}\cos\varphi_{map} \\ \dot{\psi}_{map} &= v_x\kappa_{map} \\ \delta_{map} &= L_v\kappa_{map} \end{aligned} \tag{23}$$

where θ_{map} and φ_{map} are the slope and bank angle of the road, ρ_{map} is the vertical curvature of the road, κ_{map} is the road curvature.

The most important information from the map is the curvature of road, κ_{map}. If the vehicle follows the road curve, κ_{map} could be regarded as the curvature of vehicle's trajectory. The lane changing behavior can be viewed as a noise of κ_{map}. The noise variance of κ_{map} is set as 0.032 . When κ_{map} is the curvature at current point, Equation (23) is an redundant resource of current dynamics states. When κ_{map} is the curvature at future point, the obtained accelerations and yaw rates are used to anticipate the tire forces.

4.3 Tire force prediction algorithm

The overall prediction process can be expressed by the Figure 5.

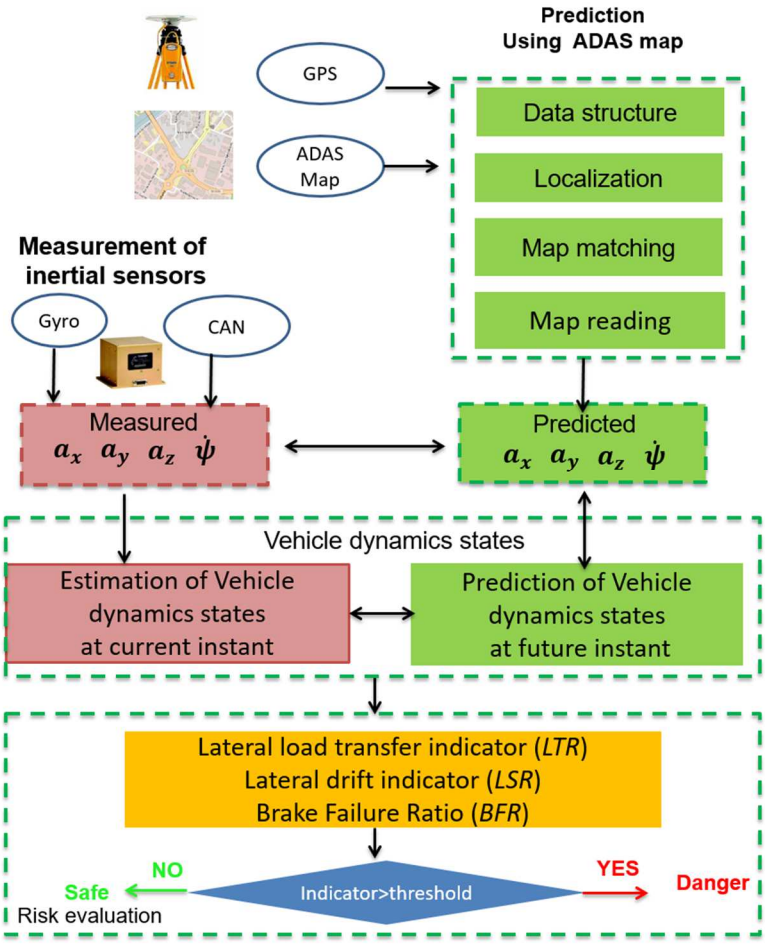

Figure 5. Overall structure of vehicle safety prediction system

The sensor measurements are used to locate the vehicle's position and identify the corresponding corridors and CPs. Then CPs can provide information about road friction coefficient which can improve the the estimation of current states. Moreover, by extracting the upcoming CPs, the estimator could anticipate the potential variation of dynamics states. Then the dynamics states of current instant and future instant will be evaluated by three indicators of safety, introduced in the above section. To simplify the prediction process, the vehicle keeps the current speed during the coming road. The prediction system will perform the risk assessment for the coming 300m road. If a potential danger is detected, the system will warn the driver to slow down.

5 Experimental validation

5.1 Vehicle description

The experimental vehicle instrumented by the laboratory, is dedicated to validate the real time estimation of vehicle's dynamics states, as shown in Figure 6. Besides the

common sensors like IMU and GPS, the vehicle is also installed with tire force transducers (RoadDyn S625), which can measure tire forces directly to provide the ground truth.

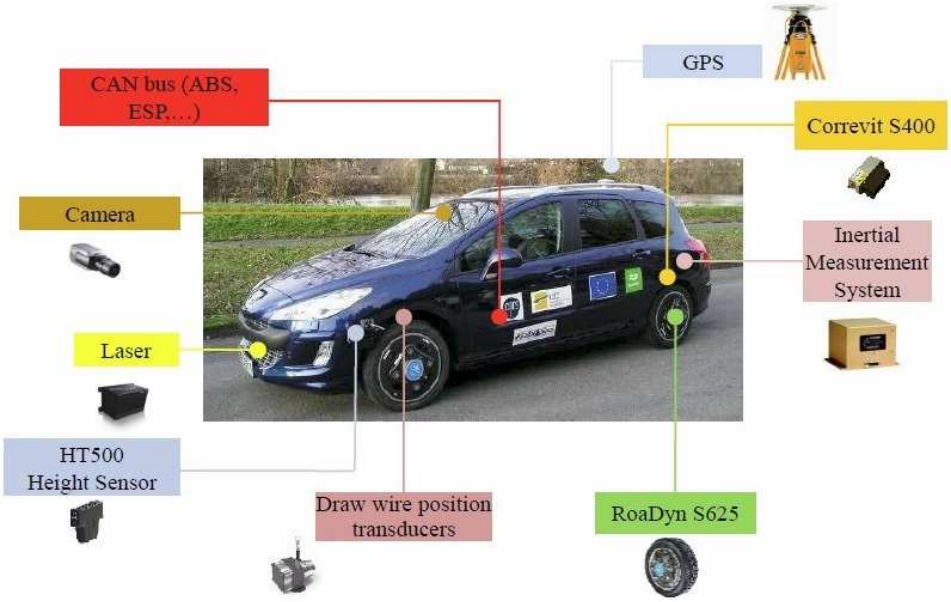

Figure 6. Experimental vehicle DYNA, equipped with different sensors

5.2 Validation of dynamics models and real-time observers

In this section, we will focus on the experimental validation of the above-mentioned observers. The input measurements of our observers are obtained from CAN bus, accelerometer, gyrometer and laser distance sensors. The force transducers are used as ground truth. In order to better present the performance of our observers in different conditions, we would like to perform three tests with different road conditions and different speeds. Three tests are designed for different objectives.

There are two tests designed for validating tire forces observers are:

Test 1: intense slalom test at 50 km/h at level ground;

Test 2: slalom test at 140 km/h at banked road.

The third test is designed to evaluate the tire force prediction algorithms.

Test 3: normal driving on the city road (for evaluating prediction algorithms) The two tests include:

All these tests are performed with our experiment vehicle DYNA on the Mortefontaine Automobile Testing and Research Centre (CERAM - Centre d'Essais et de Recherche Automobile de Mortefontaine), as shown in Figure 7.

In each test, we will present the estimation results of vertical tire forces, longitudinal tire forces and the lateral tire forces. The estimation results of the proposed new observers are noted as $O_{Fz,New}$, $O_{Fx,New}$, $O_{Fy,New}$. To make a comparison with the observers in the literature, we also developed observers based on the commonly used bicycle models. Their estimation results are noted as $O_{Fz,com}$, $O_{Fx,com}$, $O_{\beta,com}$.

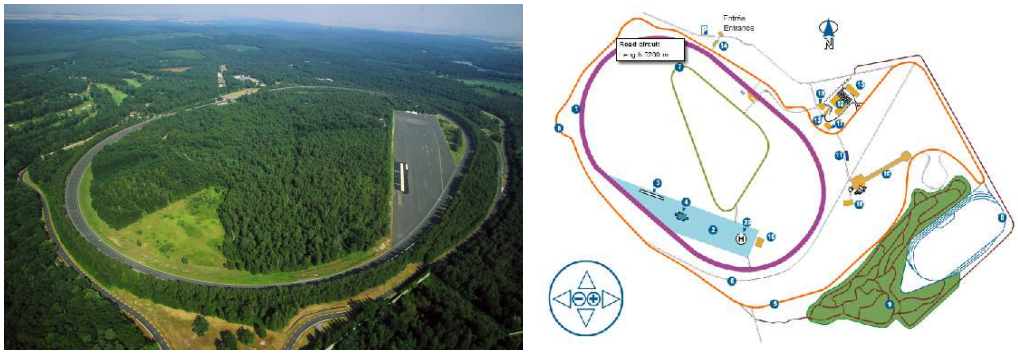

Figure 7. The trajectory of road circuit on plan

5.2.1 Intense slalom test at 50 km/h at level ground

Firstly, an extreme intense slalom test was performed. The test track was well paved and set to be dry ($\mu = 1$). The maneuver time history is illustrated in Figure 8.

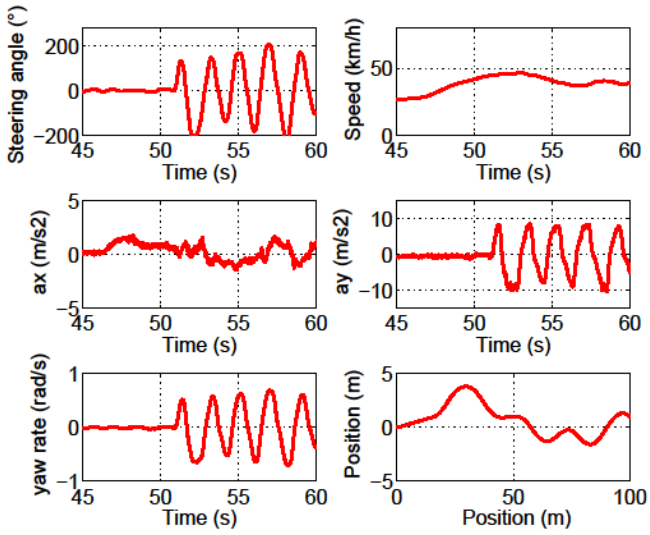

Figure 8. Maneuver time history of Test 1: Intense slalom test

During this test, the maximum lateral acceleration reached to 0.9g, average speed was about 50km/h. The steering wheel angle changed from 200° to -200° in one second, which could cause the extreme variation of the dynamics states. The slalom test is usually considered as a difficult maneuver from the estimation viewpoint, but it can better test the observer's performances.

Figure 9 demonstrates the estimation results of the vertical forces at each tire. The red lines correspond to the ground truth measured by the wheel transducer. Blue lines represent the results of the new observer that we proposed in section 3. The black dashed lines are used to illustrate the error bounds of the estimation. The value of the black dashed lines is equal to $\mathrm{Fz}_{est} \pm \sqrt{P}$, where P is the covariance obtained by Kalman filter. Green lines are the results of $O_{Fz,com}$. During the slalom maneuver, the vertical tire forces changed quickly, but our observer can follow tightly with the

measurement. Almost all the red data can be included in the error bounds $[\mathrm{Fz}_{est} - \sqrt{P}, \mathrm{Fz}_{est} + \sqrt{P}]$. The advantage of our proposed observer is obvious at the moment of each peak turning. In the Figure 9, we can see the blue line is close to the red line even at the peak points, while the green line is less accurate. It can be explained as the pitch-roll motion-based models are more sensitive to the variation of vertical force.

Figure 10 demonstrates the estimation results of the longitudinal forces at each tire. The red lines correspond to the measurement of the wheel transducer. Blue lines represent the results of the new observer that we developed in section 3. The black dashed lines represent the error bounds of our observer. The Green lines are the results based on the bicycle model and the assumption that $F_{x11} = F_{x12},\ F_{x21} = F_{x22}$. During the slalom test, the longitudinal force at front tires seems unrelated to the undulation of steering angle, while the longitudinal force at rear wheel appears a typical "slalom" characteristic. That could be explained by the fact that the experimental car is a front-drive car. The front tire forces are mainly controlled by the engines. The rear tire forces are mainly affected by the turning behaviors. The estimation provided by our new observer can tightly follow the variation of the longitudinal forces. We can find the estimation of longitudinal forces at rear wheels by using bicycle model is not so good. It is because the bicycle model is suitable for estimation of tire forces at each axle, which means the resultant longitudinal forces of rear left wheel and the rear right wheel. However, in this article, we are estimating the tire forces at each wheel rather than at each axle. With only bicycle model, we would assume the longitudinal forces at rear left and rear right wheels are the same. However, in fact, the states of left and right wheel are quite different especially during dynamic maneuvers.

Figure 11 demonstrates the estimation results of the lateral forces at each tire with the new observer, $0_{Fy,New}$, represented by blue lines. The red lines are the real data acquired by DYNA. The black lines are the error bounds. From Figure 11, we can find that the new observer showed higher accuracy at rear tires than at front tires. It is due to the model errors caused by intense slalom behavior. In this intense slalom test, the lateral forces at front tire are also greatly influenced by the steering torque, which is not considered in our model.

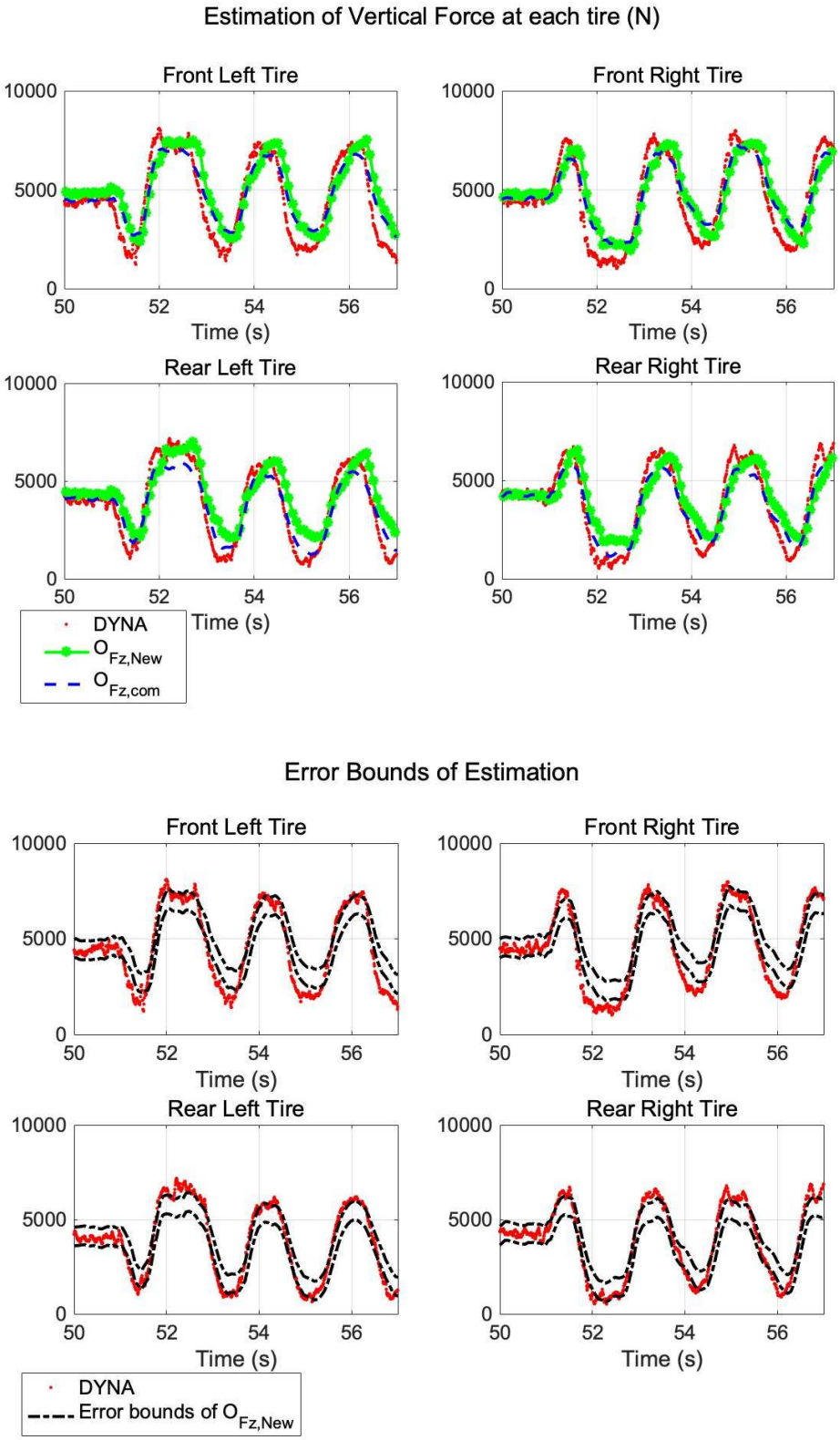

Figure 9. Test 1 (intense slalom test): Estimation of vertical force at each tire. Top four figures are the estimation results using different models; bottom four figures are the estimation error bounds to evaluate the observer's performance.

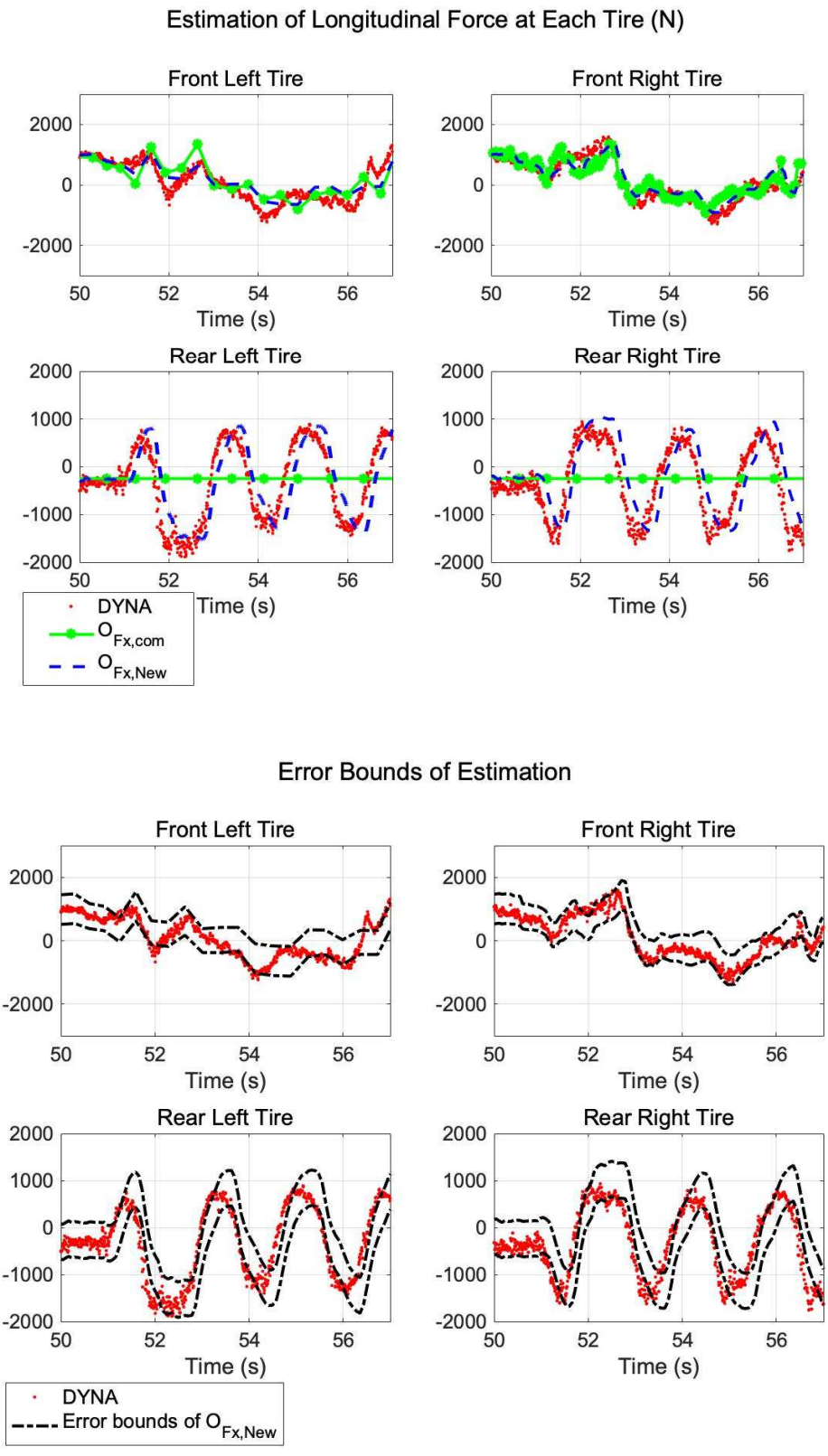

Figure 10. Test 1 (intense slalom test): Estimation of longitudinal force at each tire. Top four figures are the estimation results using different models; bottom four figures are the estimation error bounds to evaluate the observer's performance.

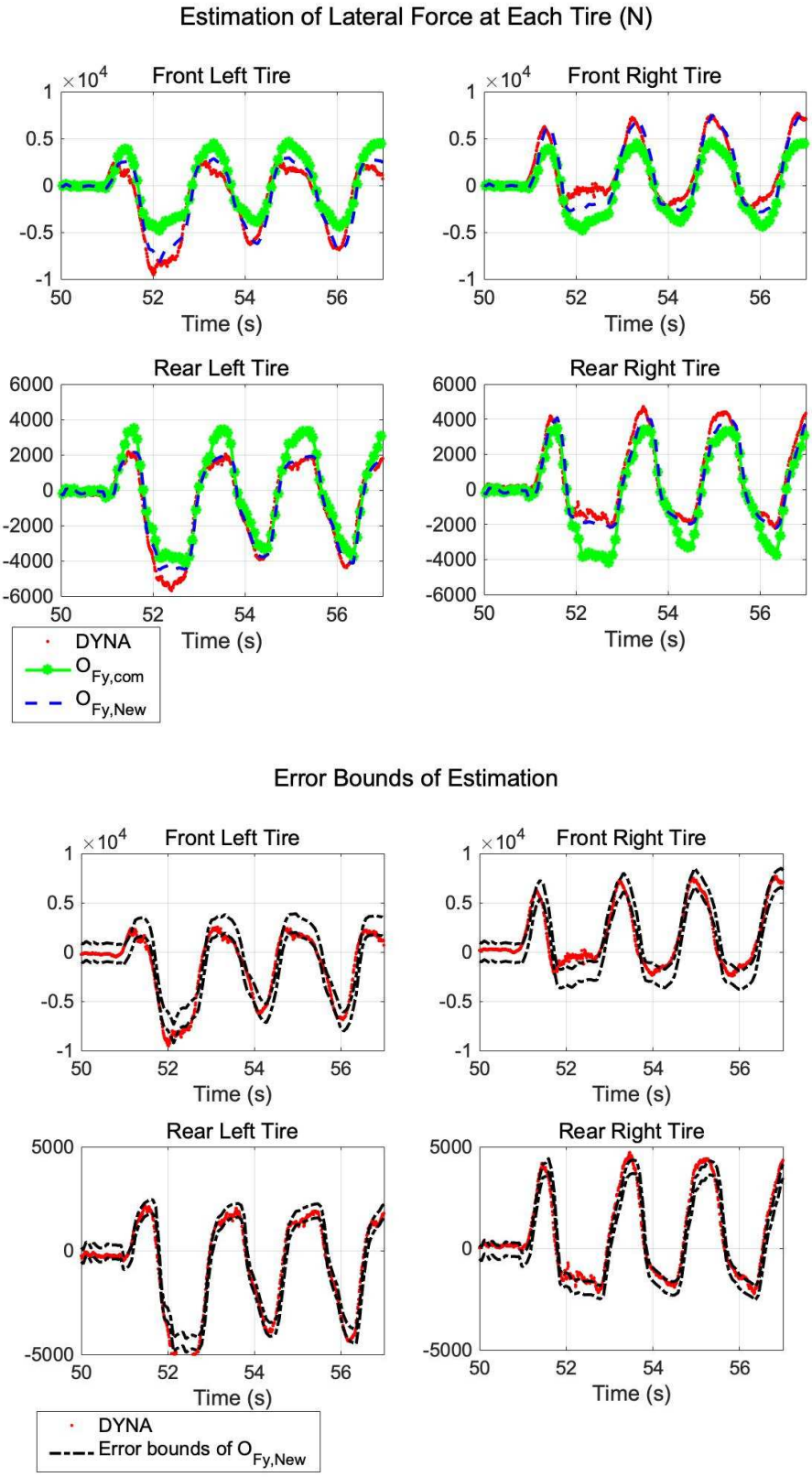

Figure 11. Test 1 (intense slalom test): Results and error bounds of the new observer for estimation of lateral forces at each tire. Top four figures are the estimation results using different models; bottom four figures are the estimation error bounds to evaluate the observer's performance.

5.2.2 Slalom test at 140 km/h on a banked road

This test is designed to validate the performance of our observers on a banked road. The test track was banked and dry ($\mu = 1$). The maneuver time history is illustrated in Figure 12. In the CERAM test center, there are three tracks: the bank angles at low track, middle track, and high track were 15°, 30° and 40° respectively. During the test, the vehicle was continuously changing from the high track to the low track.

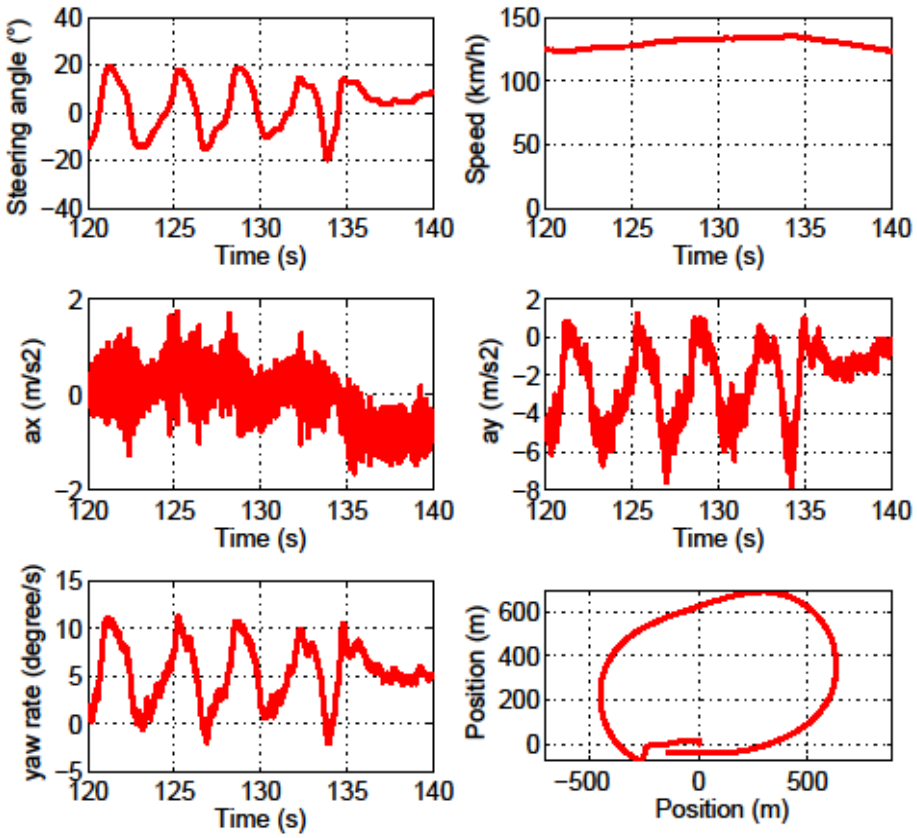

Figure 12. Maneuver time history of Test 2: Banked road slalom test

Figure 13 demonstrates the estimation result of the vertical forces at each tire. The bank angle of the road can cause the additional transfer of vertical load. However, the measured acceleration already contained the gravity component in lateral direction. As a result, the common model could also provide a good estimation of vertical force on a banked road. However, our proposed model was more accurate, as the roll and pitch motion of suspension was taken into account. The red plots in Figure 13 is the direct measurement of tire force transducers, which is the regarded as the ground truth in this article. When the vehicle is driving at 140 km/h, the vehicle is undergoing significant vibration, which is one of the reasons why the ground-truth also contains so much noises. To better evaluate the performance of our observer, we would like to filter the noise using smoothing function first and then add two new statistic indicators to evaluate the performance of our observers.

One statistic indicator is the correct rate (CR), which is calculated by the percentage

of in-error-bound estimation. This indicator is more related to accuracy, as it can show how much percentage of the estimation is close to the ground truth.

$$\mathrm{CR} = \sum_{1}^{n} \frac{est}{n}, est = \begin{cases} 1, if|F_{est} - F_{true}| \leq cov \\ 0, if|F_{est} - F_{true}| > cov \end{cases} \quad (24)$$

Where F_{est} is the estimated tire force, F_{true} is the ground truth tire force.
The other one is the Pearson correlation coefficient (PCC), which is a measure of the linear correlation between the estimation results and the direct measurement. When the PCC is very high, it means the estimation is very linear-correlated to the ground truth, which means the estimation can follow the dynamic variation of the tire force very well.

$$\mathrm{PCC} = \frac{E[(F_{est} - \overline{F_{est}})(F_{true} - \overline{F_{true}})]}{\sigma_{F_{est}} \sigma_{F_{true}}} (25)$$

Where $\sigma_{F_{est}}$ is the estimated tire force covariance, $\sigma_{F_{true}}$ is the ground truth tire force covariance.

The statistics results of Test 1 and Test 2 are given in the following Tables.

Table 3. Correct Rate of our observer and bicycle model in Test1&Test2

Correct Rate	Test1:50km/h		Test2:140km/h	
	our observer	bicycle model	our observer	bicycle model
front left tire	0.7303	0.5969	0.9289	0.9224
front right tire	0.7247	0.5913	0.8507	0.9745
rear left tire	0.9480	0.6770	0.9461	0.9828
rear right tire	0.9340	0.6208	0.9964	0.9822

Table 4. Pearson Correlation of our observer and bicycle model in Test1&Test2

Pearson Correlation	Test1:50km/h		Test2:140km/h	
	our observer	bicycle model	our observer	bicycle model
front left tire	0.9474	0.8552	0.9116	0.8764
front right tire	0.9576	0.8666	0.8747	0.8119
rear left tire	0.9778	0.9069	0.8727	0.8655
rear right tire	0.9805	0.8924	0.8547	0.8490

From the table of correct rate, we can find that in Test 1， our observers have better performance in estimation of vertical force, while in Test 2, the proposed observers had similar performance with the common observers. The different performance of our observer in Test 1 and Test 2 can be explained by that our method is more sensitive to the suspension vibration at high speed. In Test 2, the vehicle speed is about 140km/h, the measurement of vertical acceleration and vertical force contains significant noises.

From the table of Pearson correlation coefficient, we can find that in both Test 1 and Test 2, our observer had better performance in estimation of vertical force, as they had successfully followed the the sin wave profile which is caused by slalom behavior.

The advantage of our observer can be explained by that the suspension motion is considered in our vertical tire force model. The suspension motion is directly related to the vertical force.

Furthermore, we would like to explain that the plots of estimation error bounds are also good methods to demonstrate the improved performance over the existing work in the literature. We chose this method in the previous manuscript because it is a direct way to show the experimental results. Especially in our experiment, the vehicle is behaving in a slalom test. The profile of tire force is similar to a sin wave. It is a good proof to validate our observer system if our estimation result could follow the profile of real data.

Figure 14 demonstrates the estimation result of the longitudinal forces at each tire. At such a high speed (140km/h), even the direct measurement of force transducer was coupled with large noises. However, our observer provided a robust estimation about the longitudinal force, which proved the accuracy of the proposed model, T_{Fx}, on a banked road.

Figure 15 demonstrates the estimation results of the lateral forces at each tire obtained by our new observer. The proposed models, T_{Fyf} and T_{Fyr}, are reliable against the variation of road angles, which makes our new observer robust on the banked road.

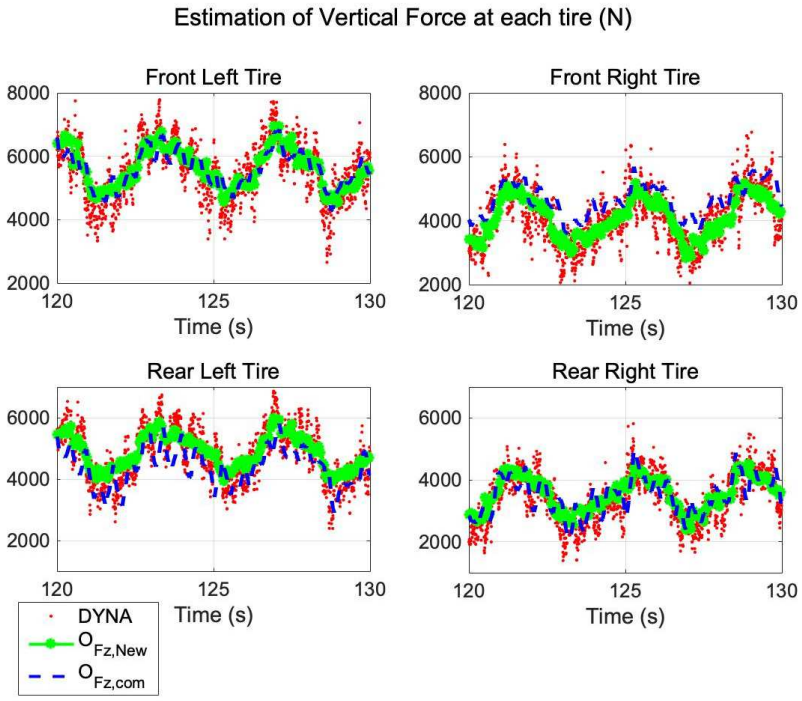

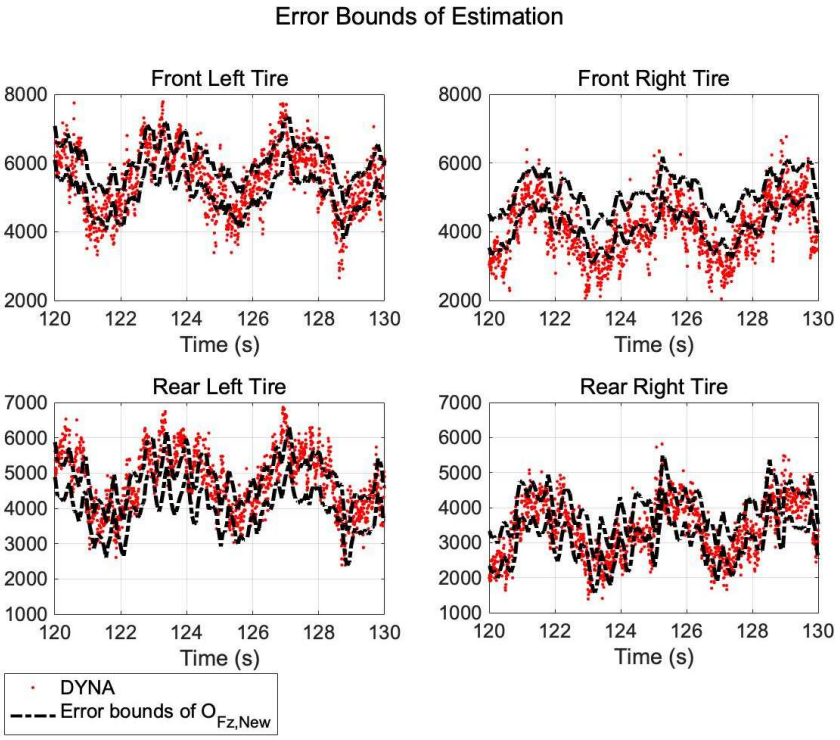

Figure 13. Test 2 (banked road slalom test): Comparison of the estimation results of vertical force at each tire. Top four figures are the estimation results using different models; bottom four figures are the estimation error bounds to evaluate the observer's performance.

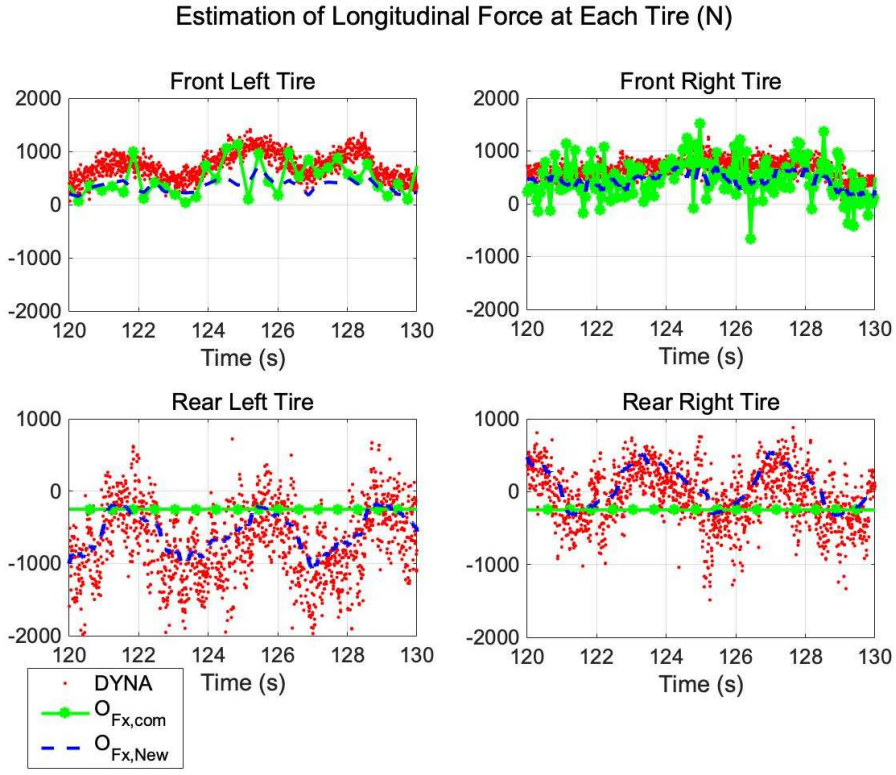

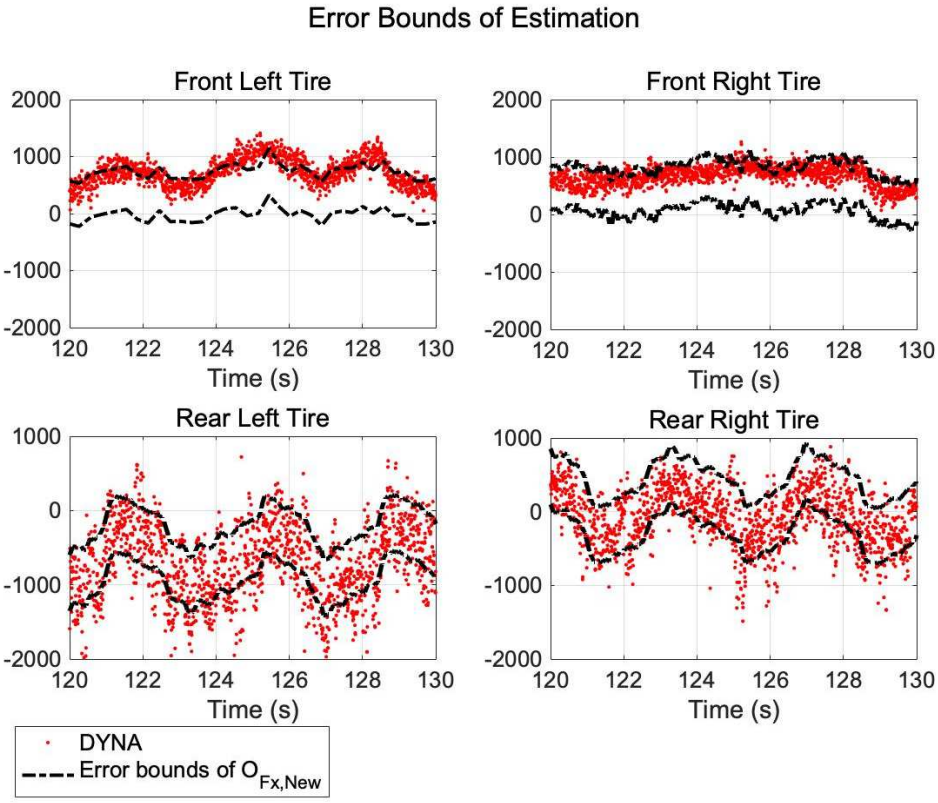

Figure 14. Test 2 (banked road slalom test): Comparison of the estimation results of longitudinal force at each tire. Top four figures are the estimation results using different models; bottom four figures are the estimation error bounds to evaluate the observer's performance.

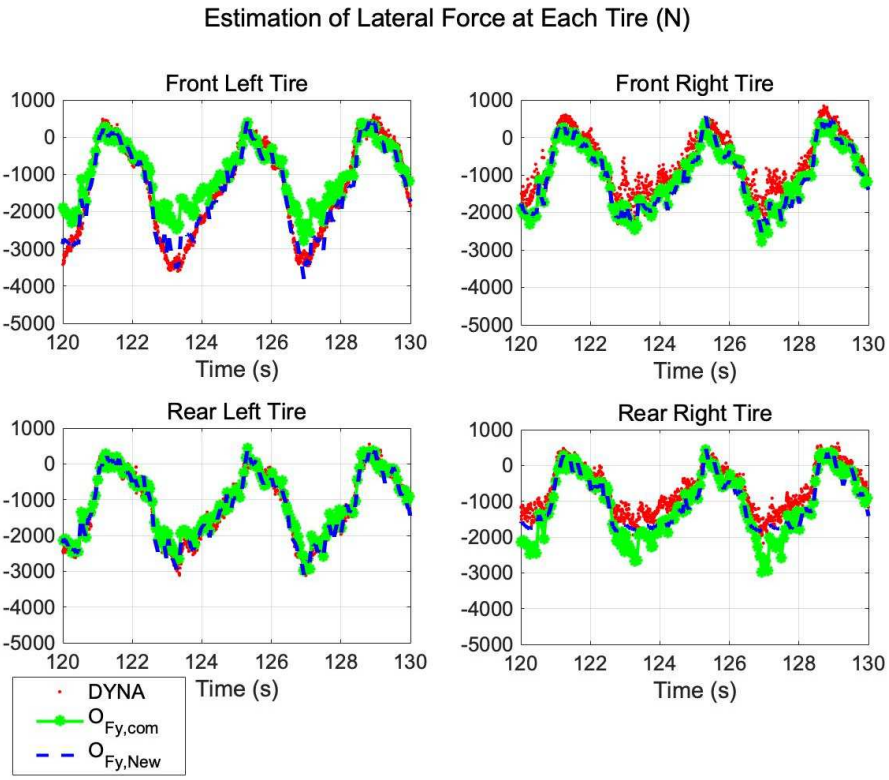

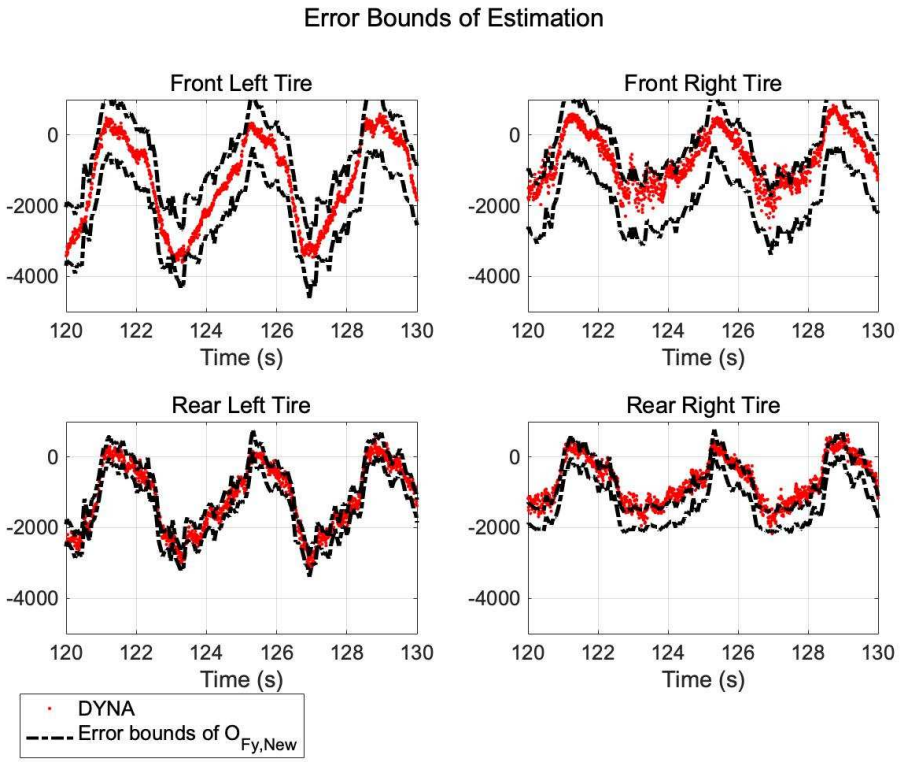

Figure 15. Test 2 (banked road slalom test): Results and error bounds of the new observer for estimation of lateral forces at each tire. Top four figures are the estimation results using different models; bottom four figures are the estimation error bounds to evaluate the observer's performance.

5.3 Validation of prediction algorithm models

We conducted the Test 3 to validate the tire force prediction algorithm. In this test, we have constructed a sample map database. Our current map database only contains the information about the road near our school, as shown in Figure 16. In the experiment, the vehicle has followed the trajectory indicated in this figure. The prediction algorithm was implemented in Matlab and validated by using the experimental data from this test.

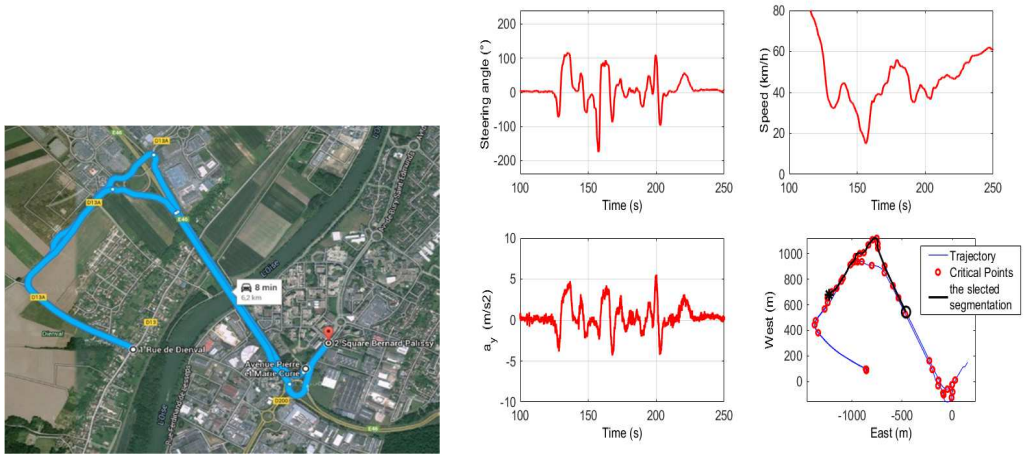

Figure 16. Vehicle's trajectory and maneuver time history: at t=150s , the vehicle is at the point of black circle, t=250s , the vehicle is at the point of black star.

In total, 53 critical points and 52 corridors were defined to describe the trajectory. More CPs were defined around the sharp turning and road intersection in order to better describe the road. Some examples of CPs and corridors are demonstrated in Table 3.

Table 5. The construction of Critical points and corridors

CP ID	x (m)	y (m)	h (m)	ψ_r (°)	κ	ρ	μ_{max}	φ (°)	θ (°)
⋮	⋮	⋮	⋮	⋮	⋮	⋮	⋮	⋮	⋮
7	-717.7	986.7	52.6	333.3	0	0	1	0	5
8	-748.1	1066.1	56.8	2.1	-0.031	0	1	0	0
9	-743.6	1103.3	57.0	343.7	0.046	0	1	0	0
⋮	⋮	⋮	⋮	⋮	⋮	⋮	⋮	⋮	⋮

Corridor Id	Id_0	Id_n	L_{corr} (m)	R_{curve}	R_{stop}
⋮	⋮	⋮	⋮	⋮	⋮
5	5	6	690	0	0
6	6	7	270	0	0
7	7	8	85	1	1
⋮	⋮	⋮	⋮	⋮	⋮

A segmentation of data (150s<t<250s) is selected due to the successive turning behaviors in this period, represented by the black line in Figure 16. The maneuver time history are presented by red lines in Figure 16. The average speed is about 50 km/h. The curvature at each critical point is illustrated by red spots in Figure 17. As we can see in this figure, the interpolation method (represented by red lines) was a simplification of real road geometry and was not always accurate. However, it effectively represented the main characteristic of the road. In the middle of Figure 17, we also demonstrated the result of localization. We have successfully estimated the travel distance, and therefore we were able to read the geometry information about the road. In the bottom of Figure 17, we presented the travel length estimation errors during the test. The travel length is obtained through the localization process, and it is the key to read map data.

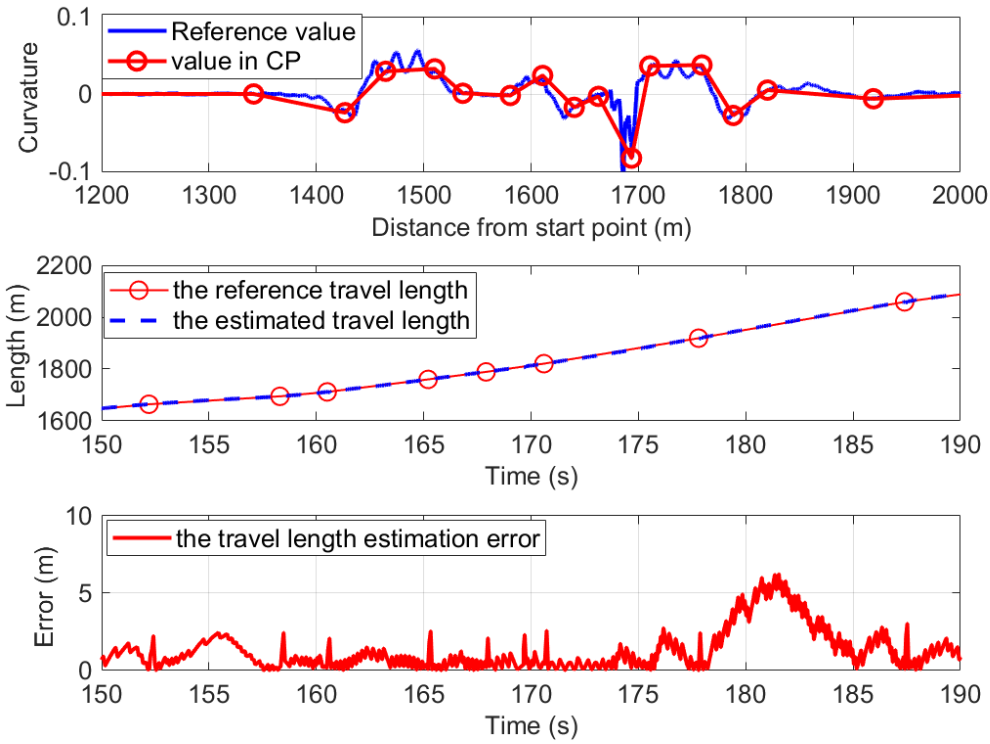

Figure 17. The value of curvature stored in each Critical Point

The obtained curvature was used to compute the value of accelerations and yaw rate with Equation 23. The comparison between inertial sensor measurement and digital map based estimation was illustrated in Figure 18. The obtained kinematic parameters were used to estimate the tire forces and sideslip angle with the observers developed in section 3. The estimation results of tire vertical and lateral forces are compared with the measurement of force transducer in Figure 19 and Figure 20. The red lines are the measurement data. The green lines represented the estimation result based on inertial sensors. The blue lines correspond to the estimation result based on the ADAS map. The accuracy of the ADAS map based method depends on the intensity of critical points and map quality. Moreover, it is also based on the condition whether the vehicle has successfully followed the planned path.

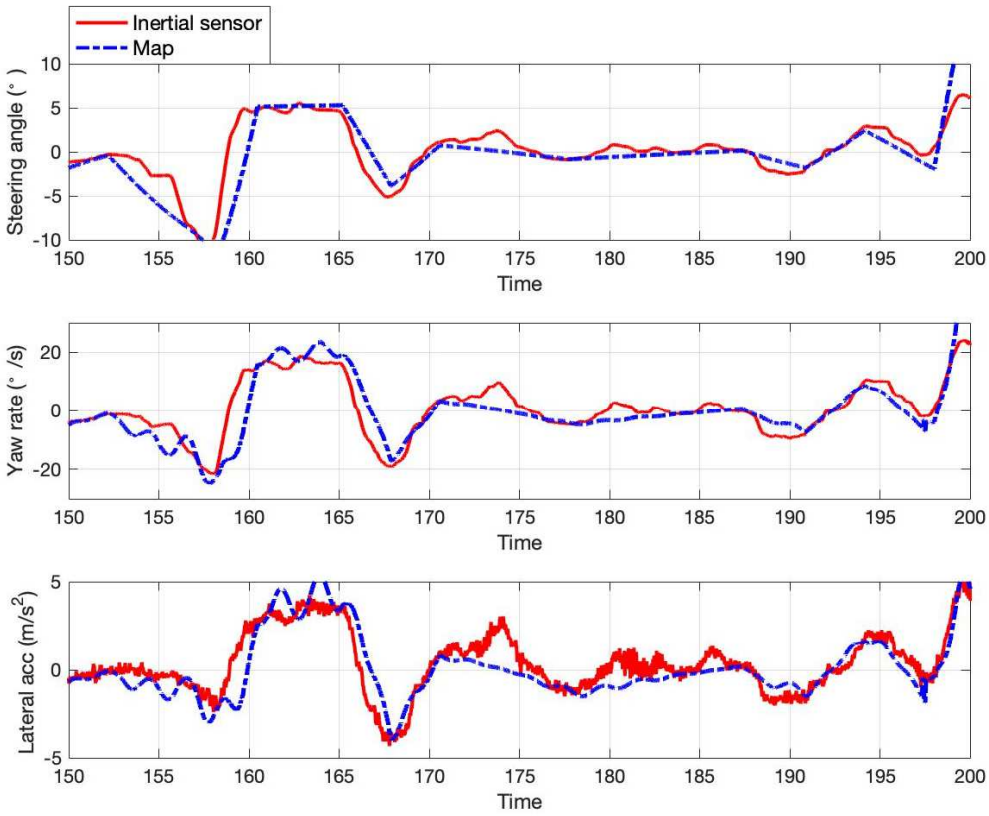

Figure 18. Comparison of lateral dynamics states estimated by inertial sensors and ADAS Map

At t=175s, the driver did a lane changing behavior, which was not in the planning and caused some errors. As demonstrated by the experimental result, the inertial sensor based method can better follow the vertical force variation, while, the map based estimation method is accurate when the vehicle is following the curve. Every time we localized the vehicle's position, we also got the curvature of the following 300 meters ahead of the vehicle's current position. Then these information was used to predict the vehicle dynamics states with Equation (12-18). And the vehicle's safety was evaluated with the index introduced by Equation (1-3). Figure 21 illustrated the prediction of vehicle's safety situation in the following 300 meters at instant t=160s and t=180s. The results showed at instant t=180s, the algorithm detected potential dangers in the upcoming path.

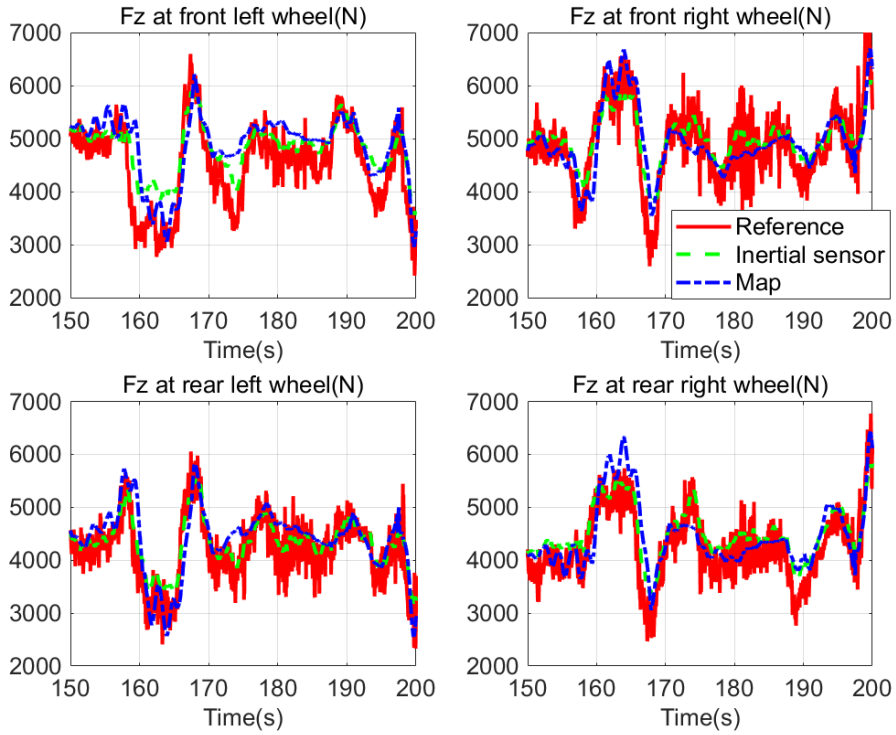

Figure 19. Estimation of vertical forces at each tire: comparison between sensor measurement and estimation

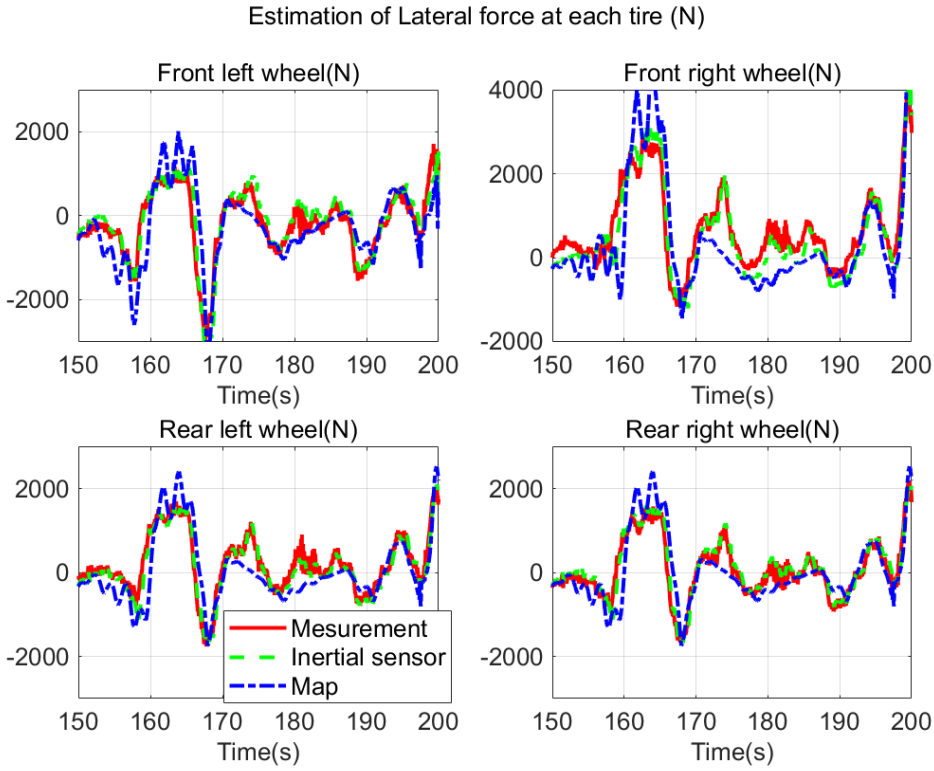

Figure 20. Estimation of lateral forces at each tire: comparison between sensor measurement and estimation

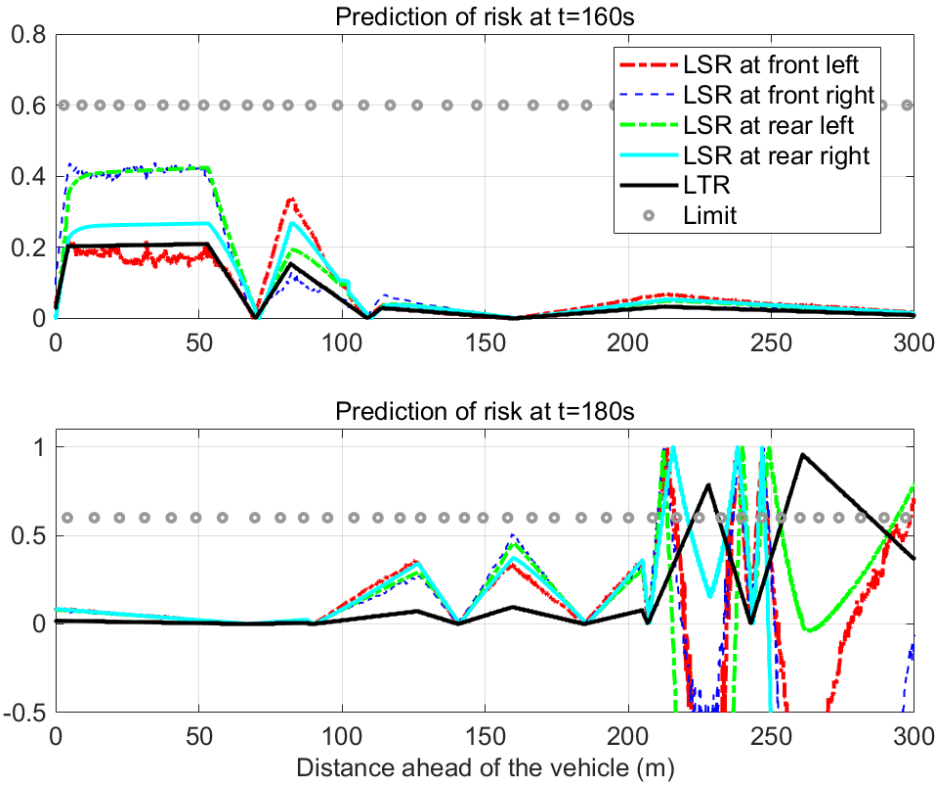

Figure 21. Prediction of vehicle safety in the following 300 meters road

6 Conclusion and Prospective

An increasing number of intelligent vehicle safety systems are being developed in university laboratories and research centers. Expansion of these intelligent systems from the early-stage development into the real-time application requires an accurate assessment of driving risk, especially when driving at high speed. In this work, we developed a driving risk assessment system using tire forces. The main difficulty in developing this system is the lack of access to information about tire forces in production cars. To solve this problem, this article has developed a set of vehicle dynamics observers, which is able to extract immeasurable tire forces from the limited measurements in real-time. The construction of an observer that can provide robust performance under all conditions is not simple. It requires accurate and efficient models and a well-developed estimation algorithm. We propose new vehicle dynamics models to consider the influence of suspension deflection and tire interactions. Furthermore, we propose the cascaded KF structure to make the estimation more reliable even in the presence of sensor noises. Another contribution of this article is to propose an algorithm to predict vehicle's dynamics states by incorporating the ADAS map. The current and future road information was obtained from the digital map to enable the assessment of driving risk in the upcoming road. Experimental results validated the proposed algorithm. With the development of high definition map, road information such as road friction coefficient is promised to be available in the near further. Therefore, the tire

force-based safety assessment process developed in this article will soon be applicable.

Future work will focus on the improvement of map quality and localization accuracy. Furthermore, we would like to develop improved warning systems which could provide maneuver suggestions besides the speed suggestion.

Acknowledgment

This work was supported by the National Key R&D Program of China (Project No. 2108YFB0105000). This work was also under the support of Project 61773234 and Project U1864203 supported by the National Natural Science Foundation of China. This work was equally supported by the International Science and Technology Cooperation Program of China under contract No. 2016YFE0102200. This work was also sponsored by Beijing Municipal Science and Technology Commission under Grant (No. D171100005117002 and Z181100005918001). This work was also funded in part by the Region Picardie VERVE project, MS2T LABEX and ROBOTEX.

References

[1] National Highway Traffic Safety Administration. (2013), "Early estimate of motor vehicle traffic fatalities for the first quarter of 2013".

[2] Bouton, N. et al. (2007), "A rollover indicator based on the prediction of the load transfer in presence of sliding: application to an All Terrain Vehicle", *IEEE Int. Conference on Robotics and Automation*, pp. 1158-1163.

[3] Imine, H. et al. (2007), "Rollover risk prediction of heavy vehicle in interaction with infrastructure", *International Journal of Heavy Vehicle Systems*, 14(3), pp. 294-307.

[4] Rajamani, R. (2012), "Vehicle Dynamics and Control", *Springer*.

[5] Reza, N. (2007), "Vehicle Dynamics Theory and Application", *Springer*.

[6] Pacejka, H. (2006), "Tire and Vehicle Dynamics", *SAE International, second edition*.

[7] Ouahi, M., Stéphant, J. & Meiezl, D. (2013), "Simultaneous observation of the wheels' torques and the vehicle dynamic state", *Vehicle System Dynamics*, 51(5), pp. 737-766.

[8] Dahmani, H., Chadli, M., Rabhi, A. & Hajjaji, A. (2013), "Vehicle dynamic estimation with road bank angle consideration for rollover detection: theoretical and experimental studies", *Vehicle System Dynamics*, 51(12), pp. 1853-1871.

[9] Wang, B., Victorino, A. & Charara, A.(2013), "State observers applied to vehicle lateral dynamics estimation: a comparison between Extended Kalman filter and Particle filter", *39th Annual Conference of the IEEE Industrial Electronics Society*.

[10] Ryu, J. & Gerdes, J. (2004), "Estimation of vehicle roll and road bank angle", *American Control Conference*, Vol. 3, pp. 2110-2115.

[11] Milliken, D., Kasprak, E., Daniel M. & Milliken W. (2003), "Race car vehicle dynamics", *SAE International*.

[12] Ghandour, R., da Cunha, F., Victorino, A., Charara, A. & Lechner, D. (2011), "A method of vehicle dynamics prediction to anticipate the risk of future accidents: Experimental validation", *14th International IEEE Conference on Intelligent Transportation Systems (ITSC)*, pp. 1692-1697.
[13] Wang, B. (2013), "State observer for diagnosis of dynamic behavior of vehicle in its environment", *PhD thesis, Universite de Technologie de Compiegne*.
[14] Nam, K., Oh, S., Fujimoto, H. & Hori, Y. (2013), "Estimation of sideslip and roll angles of electric vehicles using lateral tire force sensors through RLS and Kalman filter approaches", *Industrial Electronics, IEEE Transactions*, 60(3), pp.988-1000.
[15] Dherbomez, G., Monglon, T., Crubillé, P., Wang, B., Victorino, A., et al. (2013), "DYNA, véhicule expérimental pour la Dynamique du Véhicule", *Quatrièmes Journées des Démonstrateurs en Automatique*.
[16] Li, L., Jia, G., Ran, X., Song, J. & Wu, K. (2014), "A variable structure extended kalman filter for vehicle sideslip angle estimation on a low friction road", *Vehicle System Dynamics*, 52(2), pp.280-308.
[17] Klomp, M., Gao, Y. & Bruzelius, F. (2014), "Longitudinal velocity and road slope estimation in hybrid electric vehicles employing early detection of excessive wheel slip", *Vehicle System Dynamics*, 52(sup1), pp. 172-188.
[18] Li, X., Song, X. & Chan, C. (2014), "Reliable vehicle sideslip angle fusion estimation using low-cost sensors", *Measurement*, 51, pp. 241-258.
[19] Gadola, M., Chindamo, D., Romano, M. & Padula, F. (2014), "Development and validation of a kalman filter-based model for vehicle slip angle estimation", *Vehicle System Dynamics*, 52(1), pp. 68-84.
[20] Jiang, K., Victorino, A. & Charara, A. (2016), "Estimation and prediction of vehicle dynamics states based on fusion of OpenStreetMap and vehicle dynamics models", *IEEE Intelligent Vehicles Symposium (IV)*, pp. 208-213.
[21] Durekovic, S. & Smith, N. (2011), "Architectures of Map-Supported ADAS", *Intelligent Vehicles Symposium, IEEE*, pp. 207-211.
[22] Victorino, A., Rives, P. & Borrelly, J. (2003), "Safe navigation for indoor mobile robots, part ii: Exploration, self-localization and map building", *International Journal of Robotics Research*, 22(12), pp. 1019-1041.
[23] Aleksander, H., Brown, T. & Martens, J. (2004), "Detection of vehicle rollover", *Proceedings of the SAE World congress, Michigan, USA*.
[24] Kolansky, J. & Sandu, C. (2018), "Enhanced Polynomial Chaos-Based Extended Kalman Filter Technique for Parameter Estimation", *ASME J. of Computational and Nonlinear Dynamics*, 13(2), pp. 1-9. doi:10.1115/1.4031194.
[25] Kolansky, J. & Sandu, C. (2013), "Real-Time Parameter Estimation Study for Inertia Properties of Ground Vehicles", *The Archive of Mechanical Engineering*, LX(1), pp. 7-21. doi:10.2478/meceng-2013-0001.
[26] Kolansky, J., Sandu, C. & Els, S. (2014), "Tire-Ground Normal Force Estimation from Vehicle System Identification and Parameter Estimation", *Proc. of the ASME IDETC/CIE*, pp. 17-20.
[27] Sandu, C., Kolansky, J., Botha, T. & Els, S. (2015), "Advanced Autonomous Vehicle Design for Severe Environments", *IOS Press BV, NATO ASI*, pp. 221-241.

[28] Guo, H., Cao, D., Chen, H., Lv, C., Wang, H. & Yang, S. (2018), "Vehicle dynamic state estimation: state of the art schemes and perspectives", *IEEE/CAA Journal of Automatica Sinica,* Vol. 5 No. 2, pp. 418-431.
[29] Hashemi, E., Khosravani, S., Khajepour, A., Kasaiezadeh, A., Chen, S. & Litkouhi, B. (2017), "Longitudinal vehicle state estimation using nonlinear and parameter-varying observers", *Mechatronics,* Vol. 4328-39.
[30] Jiménez, F., Aparicio, F. & Estrada, G. (2009), "Measurement uncertainty determination and curve-fitting algorithms for development of accurate digital maps for advanced driver assistance systems", *Transportation research part C: emerging technologies,* Vol. 17 No. 3, pp. 225-239.
[31] Kissai, M., Monsuez, B., Mouton, X., Martinez, D. & Tapus, A. (2018), "Importance of Vertical Dynamics for Accurate Modelling, Friction Estimation and Vehicle Motion Control", in *2018 21st International Conference on Intelligent Transportation Systems (ITSC)*, IEEE, pp. 1370-1377.
[32] Lee, E., Jung, H. & Choi, S. (2018), "Tire Lateral Force Estimation Using Kalman Filter", *International Journal of Automotive Technology,* Vol. 19 No. 4, pp. 669-676.
[33] Li, L., Quddus, M. & Zhao, L. (2013), "High accuracy tightly-coupled integrity monitoring algorithm for map-matching", *Transportation Research Part C: Emerging Technologies,* Vol. 3613-26.
[34] Li, P. & He, J. (2016), "Geometric design safety estimation based on tire – road side friction", *Transportation Research Part C: Emerging Technologies,* Vol. 63114-125.
[35] Quddus, M. & Washington, S. (2015), "Shortest path and vehicle trajectory aided map-matching for low frequency GPS data", *Transportation Research Part C: Emerging Technologies,* Vol. 55328-339.
[36] Reina, G. & Messina, A. (2019), "Vehicle dynamics estimation via augmented Extended Kalman Filtering", *Measurement,* Vol. 133383-395.
[37] Reina, G., Paiano, M. & Blanco-Claraco, J. (2017), "Vehicle parameter estimation using a model-based estimator", *Mechanical Systems and Signal Processing,* Vol. 87227-241.
[38] Rezaeian, A., Zarringhalam, R., Fallah, S., Melek, W., Khajepour, A., Chen, S., Moshchuck, N. & Litkouhi, B. (2014), "Novel tire force estimation strategy for real-time implementation on vehicle applications", *IEEE Transactions on Vehicular Technology,* Vol. 64 No. 6, pp. 2231-2241.
[39] Sharath, M. N., Velaga, N. R. & Quddus, M. A. (2019), "A dynamic two-dimensional (D2D) weight-based map-matching algorithm", *Transportation Research Part C: Emerging Technologies,* Vol. 98409-432.

List of Keywords

$F_{z11}, F_{z12}, F_{z21}, F_{z22}$	four wheel vertical forces
μ_{max}	threshold of safe friction
$\mu_{ij,lat}$	equivalent lateral friction coefficient
$\mu_{ij,lon}$	equivalent longitudinal friction coefficient
a_y	lateral acceleration
v_x	longitudinal velocity
v_y	lateral speed
$\dot{\varphi}$	yaw rate
β_{cog}	sideslip angle of vehicle at center of gravity (COG)
δ	steering angle
I_z	vehicle's moment of inertia around z-axis
g	standard gravity on earth
ψ_v	rotation angle about the z –axis
θ_v	rotation about the y-axis (pitch angle)
φ_v	rotation about the x-axis (roll angle)
K_θ	pitch stiffness
C_θ	pitch damping coefficient
K_φ	roll stiffness
C_φ	roll damping coefficient
$M_{x,sus}$	torque about x-axis
$M_{y,sus}$	torque about y-axis
e_1	width of the front axle
e_2	width of the rear axle
L	length
$T_{Fy,f}$	transfer of lateral force at front axle
$T_{Fy,r}$	transfer of lateral force at rear axle
$T_{Fx,f}$	transfer of longitudinal force at front axle

$T_{Fx,r}$	transfer of longitudinal force at rear axle
$\hat{X}_{k+1\|k}$	state of system at time $k+1$
U	control vector
A (in Equation 10)	state transfer matrix
B	control matrix
P	covariance matrix between predicted and real values
Q	system noise covariance
K	Kalman gain matrix
H	observation transformation matrix
R	observation noise covariance
A (in Equation 11)	prediction matrix
C	observation matrix
m	dimension of the state vector
O	observability matrix
$f_{Tire,y}(\alpha, F_{wz})$	static lateral tire forces calculated by Dugoff model
F_{yf}	resultant lateral force at front axle
F_{xr}	resultant longitudinal force at rear axle
β_{best}	sideslip angle obtained by analyzing the less-slip tire
$Road_{CP0}$	road geometry information of start points of a corridor
$Road_{CP1}$	road geometry information of end points of a corridor
θ_{map}	slope angle of the road
φ_{map}	bank angle of the road
ρ_{map}	vertical curvature of the road
κ_{map}	road curvature

List of Figure captions

List of Table captions